CFD-DEM simulations of early turbulent solid-liquid mixing: Prediction of suspension curve and just-suspended speed

Bruno Blais[a], Olivier Bertrand[a], Louis Fradette[a], François Bertrand[a,*]

[a]*Research Unit for Industrial Flow Processes (URPEI), Department of Chemical Engineering, École Polytechnique de Montréal, P.O. Box 6079, Stn Centre-Ville, Montréal,QC, Canada, H3C 3A7*

Abstract

Solid-liquid mixing as a unit operation still faces considerable challenges, notably regarding the prediction of the impeller speed required to suspend the particles (N_{js}), the fraction of suspended solids and the homogeneity of the suspension at a given speed. In this work, we extend to the turbulent regime, by means of large eddy simulation (LES), a CFD-DEM model developed recently in our group for solid-liquid mixing. The resulting model is used to study the mixing of glass particles in a baffled stirred tank equipped with a down-pumping pitched blade turbine. Various characteristics of the liquid dynamics as well as the distribution and motion of the solids are investigated. The fraction of suspended solid particles predicted by the model is validated against experimental data obtained via the pressure gauge technique (PGT). Two new methods to calculate the fraction of suspended particles in a Euler-Lagrange simulation, the so-called Lagrangian suspended fraction analysis (LSFA) and the decorrelated fraction analysis (DFA) techniques are introduced. The results obtained with these two methods, as well as with many others taken from the literature, are compared to the Zwietering correlation and to the results obtained by the PGT. It is found that some techniques proposed in

*Corresponding author
Email address: francois.bertrand@polymtl.ca (François Bertrand)

the literature, namely the local concentration, the power consumption and the transient solids concentration analysis techniques, cannot be applied adequately in this case. On the other hand, the LSFA, DFA and PGT techniques are observed to predict accurately the fraction of suspended solids when compared to experimental PGT data.
Keywords: Multiphase flow; Solid-liquid mixing; Large-eddy simulation; DEM; CFD-DEM;

1. Introduction

Solid-liquid mixing operations are present in a wide range of processes. For example, stirred tanks are used as reactors for crystallization and catalytic reactions, and play a key role in the homogenization of products and the dissolution of solids in the pharmaceutical, cosmetic and food industries [1]. For many of these operations, it is sufficient to operate the impeller at the just-suspended speed (N_{js}), thus ensuring that the particles are maintained off-bottom. In such a case, the contact surface between the solid and liquid phases is near optimal and little enhancement to mass transfer can be obtained by increasing the impeller speed [2, 3]. A large body of the work in the solid-liquid mixing literature has been geared towards the prediction of the just-suspended speed, which was defined by Zwietering [4] as the speed at which no solid particles remain motionless at the bottom of the vessel for longer than 1 or 2 s. Using experimental data obtained by visual observation of the vessel bottom, Zwietering proposed the following correlation for N_{js} in RPS [1]:

$$N_{js} = S\nu_f^{0.1}\left(\frac{(\rho_p - \rho_f)\, g}{\rho_f}\right)^{0.45} d_p^{0.2} X^{0.1} D^{-0.85} \tag{1}$$

with S an empirical constant that depends on the tank configuration, ρ_f the fluid density, ρ_p the solid density, d_p the particle diameter, D the impeller diameter, ν_f the fluid

kinematic viscosity, g the gravity and X the solid mass concentration. The assessment of the just-suspended speed is important for process design and has been the the focus of considerable work, as reviewed by Kasat and Pandit [5] and Jafari *et al.* [6]. The Zwietering correlation suffers from severe limitations. The correlation has been found to be innacurate in the laminar and transitional regimes of operation [7–9], for high solids loadings [10] and for bidisperse particles [11]. Furthermore, the empiric character of the parameter S, which is very sensitive to the geometry (type of agitator, off-bottom clearance, baffle width, baffle off-bottom clearance, etc.) [10], severely limits its applicability. These limitations are shared, to varying degrees, by other correlations in the literature, such as those introduced by Nienow *et al.* [12], Narayanan *et al.* [13], Baldi *et al.* [14], Mersmann *et al.* [15], Grenville [16] and Tamburini [17].

In fact, the definition of N_{js} itself, and more importantly, the methods which have been used for measuring it, are insufficiently general. Visual observation is subjective and should not be applied for particle concentrations above $X = 8wt\%$ [18]. Although it has been used at higher solids contents, notably by Ayranci *et al.* [10] and Grenville *et al.* [16], its precision and subjectivity remain uncertain in this context. Furthermore, as noted by Tamburini *et al.* [19] and by Kasat and Prandit [5], situations occur where small amounts (<1 or 2% vol) of particles remain unsuspended and form fillet in relatively stagnant regions (e.g. below the impeller, below the baffles or near the wall-bottom junction of the tank). Kasat and Prandit [5] suggest that these small unsuspended fillets should be ignored in the determination of N_{js} by means of visual observation. However, this increases the already high subjectivity of visual observation.

Although these unsuspended particles are often insignificant from a process point of view - it is not the case for crystallization operations - they require a substantial increase

of the impeller speed to get suspended. For example, Brucato and Brucato [20] showed that for an impeller speed of 80% of that predicted by Zwietering correlation, practically all but a few particles were suspended. Similarly, Kasat and Pradit [5] observed in one of their systems that all the particles in the bulk of the flow could be suspended for impeller speed 66% to 83% of N_{js}. In the case of Brucato and Brucato [20], lowering the speed to 80% of the value of N_{js} comes with a reduction of the power consumption of $\approx 51\%$, whereas for the most extreme example discussed by Kasat and Prandit [5], this represents a reduction of $\approx 30\%$ of the original power consumption. Clearly, this can lead to considerable energy savings with little to no effect on the process efficiency.

As noted by Tamburini *et al.* [19], a large number of industrial processes are operated at speeds below N_{js} (examples can be found in the book by Oldshue [21]). Yet, all the correlations for N_{js}, such as the one proposed by Zwietering [4], are unable to predict adequately suspended conditions or the fraction of suspended solids. Surprisingly, despite the interest in operating in a partially suspended state due to the aforementioned reasons, little work has been dedicated to this issue. In fact, the core of the work on this topic has been done by Brucato *et al.* [22], Micale *et al.* [23] and Tamburini *et al.* [19, 24]. Brucato *et al.* [22] and Micale *et al.* [23] introduced the pressure gauge technique (PGT), whereby the fraction of suspended solids can be measured by means of a pressure probe at the bottom of the tank. Using this method, Micale *et al.* [23] defined the sufficiently suspended speed N_{ss} as the impeller speed required to suspend 98.2% of the particles. The pressure gauge technique was used recently by Lassaigne *et al.* [7] to investigate solid-liquid mixing for non-dilute concentrations in viscous fluids, and it was found to be a very accurate mean of measuring the speed required to suspend the particles.

The use of CFD-based models has shown to be an adequate complement to experi-

mental investigations. As reviewed by Blais *et al.* [25], mainly two types of models have been used extensively to study solid-liquid mixing : two-fluid (Euler-Euler) models and unresolved (Euler-Lagrange) CFD-DEM models. A large proportion of CFD solid-liquid mixing studies (*e.g.* [5, 19, 24, 26–37]) have been carried out using two-fluid models, which despite inherent limitations, such as the difficulty of reproducing the maximal packing fraction and the particle dynamics in dilute regions, can simulate any number of particles. However, as reviewed by Tamburini *et al.*[36], the traditional definition of N_{js} is not applicable in a continuum context (Euler-Euler) since the notion of a single particle does not make sense. Numerous procedures to obtain N_{js} have been devised for these models, among which the tangent intersection [34], the variation coefficient [38], the unsuspended solid criterion [36], and the power number [39, 40] methods. These methods were reviewed and compared by Tamburini *et al.* [36] who observed large deviations (sometimes up to 100%) among them. Note that these discrepancies are not systematic, but depend on the system studied. However, the unsuspended solid criterion and the power number methods have revealed to compare adequately to experimental data. Additionally, in another article by the same group [19], an excellent agreement was obtained between the unsuspended solid criterion method for the fraction of suspended solids and experimental data obtained via the pressure gauge technique. However, for larger particles (> 0.5 mm), the quality of the simulation results was dependent on the presence or not of correlations that take into account the effect of free stream turbulence on the drag force, such as those suggested by Brucato *et al.* [41] and Pinelli *et al.* [42].

In Euler-Lagrange models, such as unresolved CFD-DEM, the position and the velocity of each particle are tracked so that the dynamics of the solid phase is described with more accuracy than with Euler-Euler approaches. However, these models are computa-

tionally intensive and their use has been limited. Derksen [43] introduced an unresolved CFD-DEM model for solid-liquid mixing based on a hard-sphere collision model. With this model, he investigated the role of the various solid-liquid forces and concluded that drag was the dominating interaction force whereas the Saffman and Magnus lift forces played but a negligible role in the mixing dynamics. This type of model is limited to low particle concentrations since it is based on a hard-sphere collision approach and the use of regular Navier-Stokes equations. Because of this limitation to low concentrations, it cannot be used to simulate the start-up of a stirred tank. On the other hand, unresolved CFD-DEM models based on the use of the volume-averaged Navier-Stokes equations and soft-sphere DEM do not suffer from these limitations. Shao *et al.* [44] used an unresolved CFD-DEM model, combining commercial software Fluent and EDEM, to study solid-liquid mixing in a baffled tank equipped with a Rushton turbine. They investigated the evolution of the solid concentration at two impeller speeds and identified a clustering phenomenon at the tank bottom. Furthermore, contrary to Derksen [43], they concluded that the Magnus force plays an important role in the lift of the particles. The reason for this rather unexpected result will be clarified in the present work.

Despite their inherent capability to reproduce the maximal packing fraction of particles and its accurate description of the granular dynamics, unresolved CFD-DEM models have not been used to assess partially suspended conditions, the sufficiently suspended speed (N_{ss}) or the just-suspended speed (N_{js}). Recently, Blais *et al.* [25] introduced a robust unresolved CFD-DEM model for solid-liquid flows based on the CFDEM framework [45, 46], which combines Open∇FOAM for the CFD part [47] and LIGGGHTS [48, 49] for the DEM part. This model was validated in the context of solid-liquid mixing in laminar and transitional regimes using a set-up consisting of a pitched blade impeller and involving

non-dilute (10 wt%) concentrations of spherical particles. Albeit more computationally intensive than two-fluid models, this framework allowed for the determination of the fraction of suspended particles at various impeller speeds with a high degree of accuracy and with few modeling parameters or hypotheses.

In this work, the unresolved CFD-DEM model for solid-liquid mixing introduced by our group [25] is extended to the early turbulent regime of operation by means of large eddy simulation (LES). First, the flow system investigated, which consists of glass beads and a glucose solution in a baffled stirred tank equipped with a pitched blade turbine, is described and the CFD-DEM model is introduced. Then, various techniques to calculate N_{js}, N_{ss} and the fraction of suspended solids (X_{susp}) are presented. Two novel techniques to measure the fraction of suspended solids, the Lagrangian suspended fraction analysis (in two variants, LSFA-$\Delta \boldsymbol{x}$ and LSFA-Δz) and the decorrelated fraction analysis (DFA) methods are introduced. The potential of the model to predict the fraction of suspended solids is validated against experimental data obtained via the pressure gauge technique. Alternative metrics for the determination of N_{js} and N_{ss} are compared to results obtained from both existing correlations and experimental measurements. The model is also used to investigate the phase-average flow patterns, the solids distributions and, more generally, the dynamics of mixing in the stirred tank.

2. Flow system

The mixing rig consisted of a 0.365 m diameter (T) flat-bottomed, cylindrical and transparent vessel equipped with a T/3 diameter (D) down-pumping pitched blade turbine (PBT) rotating in the clockwise direction. The choice of the latter is justified by its large use in the industry for solid-liquid mixing [1]. The tank was equipped with four baffles

(W=T/10), and the clearance was set at a common value of C=T/4. The height of the liquid was equal to the tank diameter (H=T). The particles were glass beads, which are considered spherical, with a Sauter diameter ($d_{p,32}$) of 3.02 mm at a 10% w/w loading in a Newtonian glucose solution of viscosity μ of 0.0516 Pa.s. There is some evidence that for large particle diameter to impeller tank ratio (d_p/T), the just suspended speed becomes independent of the particle diameter [50]. This could possibly be the case for this set-up. The maximum impeller speed was 900 RPM, corresponding to a Reynolds number of $Re = \frac{\rho_f N D^2}{\mu} \approx 5200$ (with N in RPS). This set-up is illustrated in Figure 1. The dimensions of this mixing rig and the properties of the fluid and solid particles are summarized in Table 1.

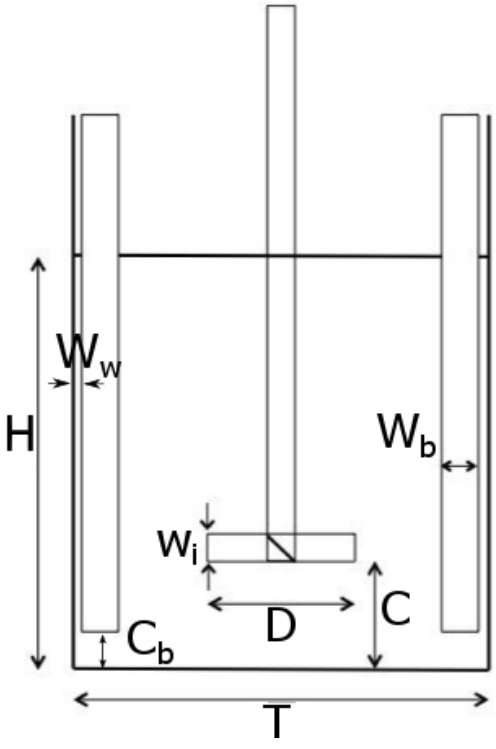

Figure 1: Experimental set-up, adapted from [51]

Table 1: Dimensions of the mixing rig and physical properties of the fluid and solid particles

Symbol	**Name**	**Value**
T	Tank diameter	0.365m
D	Impeller diameter	$\frac{T}{3}$
H	Liquid level	T
C	Off-bottom clearance	$\frac{T}{4}$
W_i	Blade width	$\frac{D}{5}$
W_b	Baffle width	$\frac{T}{10}$
W_w	Baffle spacing	$\frac{T}{14}$
C_b	Baffle bottom clearance	$\frac{T}{21}$
ρ_f	Density of the fluid	1207 kg.m^{-3}
μ	Dynamic viscosity of the fluid	0.0516 Pa.s
ρ_s	Density of the particles	2500 kg.m^{-3}
d_p	Diameter of the particles	2.66-3.5 mm
$d_{p,32}$	Sauter diameter	3.02 mm
x_s	Mass fraction of the particles	10 %
ϵ_s	Volume fraction of the particles	5.1 %

3. Model Formulation

The unresolved CFD-DEM approach consists in solving the fluid flow equations at a scale larger than that of the individual particles, while accounting for their effect on the fluid. This is achieved by using a pointwise description for the particles and by projecting both their volumes and the forces resulting from the solid-fluid interactions onto the CFD mesh, in order to calculate the void fraction and the solid-fluid momentum exchange, respectively. This projection, which can be seen as a local volume filtering techique [52], leads to a volume averaged form of the Navier-Stokes (VANS) equations [53, 54]. In order to handle the particle-particle and particle-geometry collisions, the soft-

sphere discrete element method (DEM) is used [55, 56]. These two models, which operate independently, are coupled at a regular interval - for instance at each CFD iteration - and the positions and velocities of the particles are used to update the solid-fluid coupling. The model presented in this work can be seen as an extension of our recent work [25, 51] to turbulent flows using large eddy simulation (LES). First, we present the equations for the DEM, then the equations for the CFD part and, finally, the two-way coupling between the particles and the fluid.

3.1. Governing equations for the solid-phase (DEM)

In the discrete element method (DEM), the position and velocity of each particle are tracked, and collisions are handled by allowing minute overlaps between spheres. This overlap is decomposed into normal and tangential directions, and used within contact models that contain elastic and dissipative components, thus allowing for the treatment of inelastic particle-particle collisions [55, 56].

As a result of Newton's second law of motion, the governing equations for the translational ($\boldsymbol{v}_i$) and rotational ($\boldsymbol{\omega}_{p,i}$) motion of particle i can be written as [48]:

$$m_i \frac{d\boldsymbol{u}_i}{dt} = \sum_j \boldsymbol{f}_{c,ij} + \sum_k \boldsymbol{f}_{lr,ik} + \boldsymbol{f}_{pf,i} + \boldsymbol{f}_{g,i} \tag{2}$$

$$I_i \frac{d\boldsymbol{\omega}_{p,i}}{dt} = \sum_j (\boldsymbol{M}_{t,ij} + \boldsymbol{M}_{r,ij}) \tag{3}$$

where m_i is the mass of particle i, I_i the moment of inertia of particle i, $\boldsymbol{f}_{c,ij}$ the con-

tact forces between particles i and j, $\boldsymbol{f}_{lr,ik}$ the non-contact (long-range) forces between particles i and k, $\boldsymbol{f}_{pf,i}$ the particle-fluid interaction forces, $\boldsymbol{f}_{g,i}$ the gravitational force ($\boldsymbol{f}_{g,i} = m_i\boldsymbol{g}$), and $\boldsymbol{M}_{t,ij}$ and $\boldsymbol{M}_{r,ij}$ the tangential and rolling friction torques acting on particles i and j. In the present work, non-contact forces, such as the electrostatic or van Der Waals forces are neglected due to the size and nature of the particles (3 mm glass beads). The expression for the particle-fluid interaction forces depends on which interactions are taken into account (drag, virtual mass, lift, etc.). This is discussed in Section 3.4.

The contact forces between two particles are split into normal ($\boldsymbol{f}_{cn,ij}$) and tangential ($\boldsymbol{f}_{ct,ij}$) [56] components:

$$\boldsymbol{f}_{c,ij} = \boldsymbol{f}_{cn,ij} + \boldsymbol{f}_{ct,ij} = -k_{n,ij}\boldsymbol{\delta}_{n,ij} - \gamma_{n,ij}\dot{\boldsymbol{\delta}}_{n,ij} - k_{t,ij}\boldsymbol{\delta}_{t,ij} - \gamma_{t,ij}\dot{\boldsymbol{\delta}}_{t,ij} \tag{4}$$

where $k_{n,ij}$ and $k_{t,ij}$ are the normal and tangential stiffness coefficients, $\gamma_{n,ij}$ and $\gamma_{t,ij}$ the normal and tangential damping coefficients, $\boldsymbol{\delta}_{n,ij}$ and $\boldsymbol{\delta}_{t,ij}$ the normal and tangential overlaps, and $\dot{\boldsymbol{\delta}}_{n,ij}$ and $\dot{\boldsymbol{\delta}}_{t,ij}$ their derivatives with respect to time.

In the present work, a model proposed by Tsuji *et al.* [57] based on the Hertz theory [58, 59] is used for the normal forces. For the tangential force, the Mindlin model [60, 61] is used. These models are combined to link the stiffness and the damping coefficients to the Young's modulus of the material (Y), the Poisson ratio (ν) and the coefficient of restitution (e_r), using the equations described in Table 2. The tangential overlap $\boldsymbol{\delta}_{t,ij}$ is

truncated by means of Coulomb's law to ensure that $\boldsymbol{f}_{ct,ij} \leq -\mu_{s,ij} \left|\boldsymbol{f}_{cn,ij}\right| \frac{\boldsymbol{\delta}_{t,ij}}{|\boldsymbol{\delta}_{t,ij}|}$.

Table 2: Equations for the DEM model

Parameter	Equation
Normal stiffness	$k_{n,ij} = \frac{4}{3} Y^*_{ij} \sqrt{R^*_{ij} \delta_{n,ij}}$
Tangential stiffness	$k_{t,ij} = 8 G^*_{ij} \sqrt{R^*_{ij} \delta_{n,ij}}$
Normal damping	$\gamma_{n,ij} = -2\sqrt{\frac{5}{6}} \frac{\ln(e_r)}{\sqrt{\ln^2(e_r)+\pi^2}} \sqrt{\frac{2}{3} k_n m^*_{ij}}$
Tangential damping	$\gamma_{t,ij} = -2\sqrt{\frac{5}{6}} \frac{\ln(e_r)}{\sqrt{\ln^2(e_r)+\pi^2}} \sqrt{k_t m^*_{ij}}$
Coulomb friction force	$\boldsymbol{f}_{ct,ij} \leq -\mu_{s,ij} \left\|\boldsymbol{f}_{cn,ij}\right\| \frac{\boldsymbol{\delta}_{t,ij}}{\|\boldsymbol{\delta}_{t,ij}\|}$
Torque by tangential forces	$\boldsymbol{M}_{t,ij} = \boldsymbol{r}_i \times (\boldsymbol{f}_{ct,ij})$
Rolling friction torque	$\boldsymbol{M}_{r,ij} = -\mu_{r,ij} \left\|\boldsymbol{f}_{cn,ij}\right\| \frac{\boldsymbol{\omega}_{p,ij}}{\|\boldsymbol{\omega}_{p,ij}\|} R^*_{ij}$
Equivalent mass	$\frac{1}{m^*_{ij}} = \frac{1}{m_i} + \frac{1}{m_j}$
Equivalent radius	$\frac{1}{R^*_{ij}} = \frac{1}{R_i} + \frac{1}{R_j}$
Equivalent Young's modulus	$\frac{1}{Y^*_{ij}} = \frac{\left(1-\nu_i^2\right)}{Y_i} + \frac{\left(1-\nu_j^2\right)}{Y_j}$
Equivalent shear modulus	$\frac{1}{G^*_{ij}} = \frac{2(2+\nu_i)(1-\nu_i)}{Y_i} + \frac{2(2+\nu_j)(1-\nu_j)}{Y_j}$
Sliding friction coefficient	$\mu_{s,ij}$
Rolling friction coefficient	$\mu_{r,ij}$
Distance to contact point for particle i	$\boldsymbol{r}_i$
Radius of particle i	R_i

3.2. Governing equations for the liquid flow (CFD)

Form A (or set II using the notation of Zhou *et al.* [54]) of the incompressible volume-averaged Navier-Stokes (VANS) equations are solved for the liquid phase [62]. A filtering kernel [63] is applied to these equations, leading to the following filtered VANS equations:

$$\frac{\partial \epsilon_f}{\partial t} + \nabla \cdot (\epsilon_f \bar{\boldsymbol{u}}) = 0 \tag{5}$$

$$\frac{\partial \left(\rho_f \epsilon_f \bar{\boldsymbol{u}}\right)}{\partial t} + \nabla \cdot (\rho_f \epsilon_f \bar{\boldsymbol{u}} \otimes \bar{\boldsymbol{u}}) = -\epsilon_f \nabla \bar{p} + \nabla \cdot \boldsymbol{\tau} + \nabla \cdot \boldsymbol{\tau_{sgs}} - \boldsymbol{F}_{pf} \tag{6}$$

where ϵ_f is the void fraction, ρ_f the density of the fluid, $\bar{p}$ the filtered pressure and $\bar{\boldsymbol{u}}$ the filtered velocity. The viscous stress tensor $\boldsymbol{\tau}$ is defined as:

$$\boldsymbol{\tau} = \epsilon_f \mu \left(2\bar{\boldsymbol{S}} - \frac{2}{3} \left(\nabla \cdot \bar{\boldsymbol{u}} \right) \boldsymbol{\delta}_k \right) \tag{7}$$

$$\bar{\boldsymbol{S}} = \frac{1}{2} \left(\nabla \bar{\boldsymbol{u}} \right) + \left(\nabla \bar{\boldsymbol{u}} \right)^T \tag{8}$$

where μ is the dynamic viscosity of the fluid, $\boldsymbol{\delta}_k$ the identity tensor and $\bar{\boldsymbol{S}}$ the strain-rate tensor of the resolved velocity. In the present work, the sub-grid scale Reynolds stress tensor $\boldsymbol{\tau_{sgs}}$, which is brought into play due to the filtering of the advection term in the VANS equations, is based on the Smagorinsky model [64]:

$$\boldsymbol{\tau}_{sgs} = \epsilon_f \mu_t \left(2\bar{\boldsymbol{S}} - \frac{2}{3} \nabla \cdot \bar{\boldsymbol{u}} \boldsymbol{\delta}_k \right) \tag{9}$$

In this equation, μ_t is the subgrid-scale eddy viscosity given by:

$$\mu_t = C_s \rho_f \Delta^2 \left| \bar{S} \right| \tag{10}$$

where $C_s = 0.17$ is the Smagorinsky constant [65], Δ is the grid size and $\left| \bar{S} \right| = \sqrt{\bar{\boldsymbol{S}} : \bar{\boldsymbol{S}}}$. Note that the value $C_s = 0.17$ was established for free turbulence away from the walls. This could lead to some overdamping of the turbulent structures for the Reynolds numbers considered in this work.

The momentum exchange (or coupling) term from the particles to the fluid $\boldsymbol{F}_{pf}$ can

be broken down into the following components:

$$\boldsymbol{F}_{pf} = \frac{1}{\Delta V} \sum_{i}^{n_p} \boldsymbol{f}_{pf,i} - \boldsymbol{f}_{\nabla p,i} - \boldsymbol{f}_{\nabla \cdot \boldsymbol{\tau},i} - \boldsymbol{f}_{\mathrm{Ar},i} \tag{11}$$

$$\boldsymbol{f}_{pf,i} = \boldsymbol{f}_{d,i} + \boldsymbol{f}_{\nabla p,i} + \boldsymbol{f}_{\nabla \cdot \boldsymbol{\tau},i} + \boldsymbol{f}_{\mathrm{Ar},i} + \boldsymbol{f}_{\mathrm{vm},i} + \boldsymbol{f}_{B,i} + \boldsymbol{f}_{\mathrm{Saff},i} + \boldsymbol{f}_{\mathrm{Mag},i} \tag{12}$$

where n_p is the number of particles and $\boldsymbol{f}_{pf,i}$ is the sum of all solid-liquid interaction forces involving particle i: drag ($\boldsymbol{f}_{d,i}$), pressure gradient ($\boldsymbol{f}_{\nabla p,i}$), viscous force ($\boldsymbol{f}_{\nabla \cdot \boldsymbol{\tau},i}$), Archimedes force ($\boldsymbol{f}_{\mathrm{Ar},i}$), virtual mass ($\boldsymbol{f}_{\mathrm{vm},i}$), Basset force ($\boldsymbol{f}_{B,i}$), Saffman lift ($\boldsymbol{f}_{\mathrm{Saff},i}$) and Magnus lift ($\boldsymbol{f}_{\mathrm{Mag},i}$). We recall that the effect of the pressure, viscous and Archimedes forces are included directly into the continuous VANS equations, which explains why they are removed from the $\boldsymbol{F}_{pf}$ term.

These equations are solved here using a pressure implicit with splitting of operators (PISO) scheme [66] that was extended to the VANS equations and verified using the method of manufactured solutions, by Blais and Bertrand [67]. A second-order centered scheme is combined with a second-order implicit backward time integration scheme, thus preserving the second-order accuracy of the overall scheme for pressure and velocity in both space and time.

3.3. Rotating impeller

The PISO-IB method, a semi-implicit immersed boundary method developed by Blais *et al.* [51] is used to take into account the rotating impeller. This immersed boundary

method is inserted directly within the PISO scheme for the VANS equations and only requires one single static locally refined mesh. This way, the rotating impeller can be modelled without using sliding mesh techniques, which has the advantage of preserving the mesh topology, thus leading to a faster detection of the particle location within the mesh as well as to a more stable void fraction field.

3.4. Solid-liquid coupling

In CFD-DEM, the solid-liquid interaction forces (or coupling), as presented in the previous subsection, are modeled by the expressions given in Table 3. The value of the velocity, viscous stress tensor and pressure are obtained via linear interpolation using the neighbouring cells.

In particular, the expressions for the Saffman lift force proposed by McLaughin [71] and subsequently by Mei [69] were derived for small values of the particle Reynolds number (Re_p). However, it was shown to be reasonable for $Re_p < 50$ and $w^* < 0.8$ by Loth [72], values which should not be exceeded in the bulk of the flow (except maybe close to the impeller blades) for the system studied in the present work due to the maximal impeller speed considered (900 RPM). Note that the impact of the void fraction (ϵ_f) on this lift force has not been investigated and it is assumed in the present work that the expression proposed by Mei [69] remains valid with increasing particle concentrations.

A drag force model from Rong *et al.* [68] is used without a correction term for the

Table 3: Expressions for the solid-liquid interaction forces

Force	Equation
Pressure gradient - $\boldsymbol{f}_{\nabla p,i}$	$-V_p \nabla \bar{p}$
Viscous force - $\boldsymbol{f}_{\nabla\cdot\boldsymbol{\tau},i}$ [56]	$-V_p \nabla \cdot \boldsymbol{\tau}$
Drag -$\boldsymbol{f}_{d,i}$	$\frac{\pi}{8} C_D d_p^2 \rho_f \left\|\bar{\boldsymbol{u}} - \boldsymbol{v}_i\right\| \left(\bar{\boldsymbol{u}} - \boldsymbol{v}_i\right) \epsilon_f^{2-\beta(\epsilon_f, Re_p)}$
Rong model [68]	with $\boldsymbol{v}_i$ the velocity of particle i
	$C_D = \left(0.63 + \frac{4.8}{\sqrt{Re_p}}\right)^2$,
	$\beta\left(\epsilon_f, Re_p\right) = 2.65\left(\epsilon_f + 1\right) - \left(5.3 - 3.5\epsilon_f\right)\epsilon_f^2 e^{-\frac{\left(1.5 - \log {Re_p}^2\right)}{2}}$,
	and $Re_p = \frac{\rho_f d_p \left\|\bar{\boldsymbol{u}} - \boldsymbol{v}_i\right\|}{\mu}$
Saffman Lift - $\boldsymbol{f}_{\text{Saff},i}$	$J^* 1.614 \rho_f^{\frac{1}{2}} \mu_f^{\frac{1}{2}} \left(\bar{\boldsymbol{u}} - \boldsymbol{v}_i\right) \times \frac{\boldsymbol{w}}{\left\|\boldsymbol{w}\right\|^{\frac{1}{2}}}$
Mei model [69–71]	with $J^* = 0.3\left(1 + \tanh\left(\frac{5}{2}\left(\log_{10}\sqrt{\frac{w^*}{Re_p}} + 0.191\right)\right)\right)$
	$\left(\frac{2}{3} + \tanh\left(\sqrt{\frac{w^*}{Re_p}} - 1.92\right)\right)$,
	$\boldsymbol{w} = \nabla \times \bar{\boldsymbol{u}}$,
	$w^* = \frac{\left\|\boldsymbol{w}\right\| d_p}{\left\|\bar{\boldsymbol{u}} - \boldsymbol{v}_i\right\|}$,

effect of free stream turbulence on the drag coefficient. This correction, which models the impact on unresolved turbulent structures on the drag coefficient is necessary in Euler-Euler simulations at high Reynolds number where the mesh size is significantly larger than the particle diameter, as shown for example by Tamburini *et al.* [19]. However, following the work of Capeceletro *et al.* [52] and considering the smaller mesh size to particle size ratio and the lower Reynolds numbers considered in our work, such a correction was not added to our model.

It must be noted that the Basset ($\boldsymbol{f}_B$), Magnus lift ($\boldsymbol{f}_{Mag}$) and virtual mass ($\boldsymbol{f}_{vm}$) forces are neglected in the present study.

The Basset force, sometimes referred to as the history force due to its time integral form, is due to the formation of a viscous boundary layer around a particle. For a single particle, it is written as [73]:

$$\boldsymbol{f}_{B,i} = \frac{3}{2}\pi\mu d_p^2 \int_0^t \frac{\frac{d(\boldsymbol{u}-\boldsymbol{v}_i)}{d\theta}}{\pi\nu\left(t-\theta\right)^{\frac{1}{2}}} d\theta \tag{13}$$

Since it results from the integration in time along the particle trajectory, the calculation of the Basset force is computationally challenging. This force could have a significant impact only close to the impeller region due to the strong velocity fluctuations that occur in this region [43]. For the geometry considered in the present work, a pitched blade turbine (PBT) with 4 blades, the frequency ξ of the time-varying flow field close to the impeller can be estimated as $\xi = 4N$ with N in revolutions per second. Thus, the

ratio between the Basset force and the Stokes drag (for $Re_p < 1$) can be estimated as $\frac{|\boldsymbol{f}_B|}{|\boldsymbol{f}_d|} = 0.1\sqrt{\frac{d_p^2 \mu \xi}{\rho_f}}$, which is 0.5 for the maximum impeller speed (900RPM) considered in this work. However, for this velocity, the particle Reynolds number $Re_p = \frac{\rho_f d_p |\boldsymbol{u}-\boldsymbol{v}|}{\mu}$ in the region of the impeller for the fluid and particle properties given in Table 1 is of the order of 50. Therefore, the Stokes law does not apply and the drag coefficient is significantly higher than what is predicted by the Stokes formula. This indicates that the real ratio $\frac{|\boldsymbol{f}_B|}{|\boldsymbol{f}_d|} << 1$ and that the Basset force can be neglected. Finally, we note that the above expression for the Basset force is valid only for a single particle, and the effect on this force of non-dilute concentrations of particles or the Reynolds number has, to our knowledge, not been studied. In other words, it is unknown whether the presence of other particles increases or decreases the value of the Basset force felt by a particle.

The Magnus lift forc is generated by the angular velocity of a particle, as illustrated in Figure 2. For a single particle, it is given by the following expression [74]:

$$\boldsymbol{f}_{M,i} = \frac{\pi}{8} d_p^2 \rho_f C_M \left|\boldsymbol{u} - \boldsymbol{v}_i\right| \frac{(\boldsymbol{w} - 2\boldsymbol{\omega}_p) \times (\boldsymbol{u} - \boldsymbol{v}_i)}{|\boldsymbol{w} - 2\boldsymbol{\omega}_p|} \tag{14}$$

where $\boldsymbol{w}$ is the vorticity of the fluid and C_M the Magnus coefficient, which depends on Re_p and on the rotational Reynolds number $Re_R = \frac{\rho_f d_p^2 \left|\frac{1}{2}\boldsymbol{w} - \boldsymbol{\omega}_{p,i}\right|}{\mu}$.

The integration of the Magnus lift force within unresolved CFD-DEM simulations is a complex issue. Although the angular momentum is solved for each particle, the angular motion of the particles (and that of the fluid around it) is not felt by the fluid since the

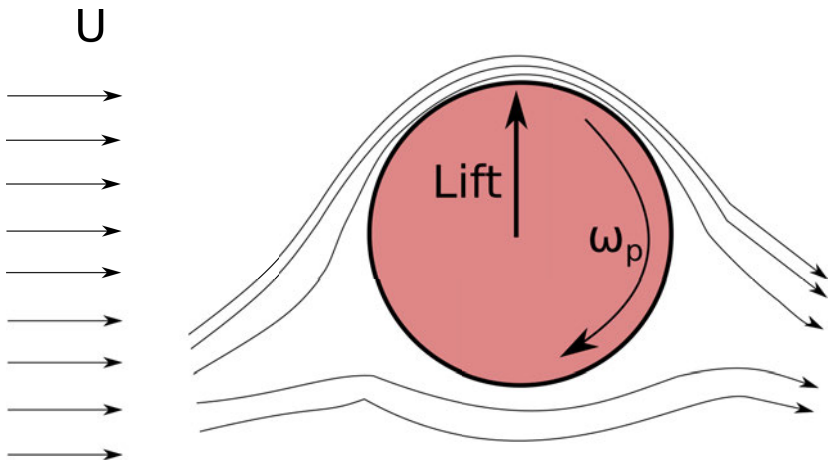

Figure 2: Scheme of the Magnus lift force due to the perturbation of the mean flow U caused by the angular motion ω_p of a particle

latter is solved at a scale coarser than that of the particles. Moreover, no conservation equation is solved for the vorticity. Consequently, in standard CFD-DEM simulations, the angular velocity of a particle will change only when it comes into contact with an element of the geometry or with another particle. If the Magnus lift force is kept in Eq. (12), the angular momentum of the particle will be one-way coupled with the translational momentum of the particle and that of the fluid. Therefore, a freely rotating particle will affect its translational momentum and that of the fluid while maintaining a constant angular momentum, a behavior that is not physical. One way around this would be to add a solid-liquid term on the right-hand side of Eq. (3) to account for the viscous (or turbulent) dissipation of the angular momentum of the particle due to the presence of the liquid. This may explain why some investigations from the literature, which did not

include such a force (*e.g.* Shao *et al.* [44]), have reported surprisingly large contributions of the Magnus force to the solid-liquid mixing dynamics.

Derksen [43] remedied this shortcoming by introducing a so-called solid-liquid torque based on the analytical solution of the flow of a particle rotating in a viscous fluid, as calculated by Dennis *et al.* [75]. The resulting solid-fluid torque is given by:

$$\boldsymbol{M}_{i,pf} = \pi \mu d_p^3 \left(\frac{1}{2} \boldsymbol{\omega} - \boldsymbol{\omega}_p \right) \tag{15}$$

This torque can be added on the right hand side of Eq (3). However, since we do not solve explicitely for the angular momentum of the fluid, this term cannot be applied on the VANS equations, thus breaking the two-way coupling. Furthermore, we note that the effect of the void fraction on the Magnus lift force and that of the Reynolds numbers (Re_p and Re_R) on this solid-liquid torque have not been established. In fact, the presence of neighbouring particles is expected to affect the magnitude of the solid-liquid torque significantly, as it does for drag (as can be seen in the Rong drag model in Table (3)). In this case, the angular velocity of the particles is likely to relax in a very short time, decreasing considerably the effect of the Magnus lift force. Clearly, the issue of the angular momentum coupling in unresolved Euler-Lagrangian models requires further investigation, which is out of the scope of the present work. Consequently, following along the lines of Arolla and Desjardins [76], we did not consider in our CFD-DEM model the Magnus lift force.

The virtual mass force manifests itself as additional inertia due to the displacement of the fluid caused by the motion of a particle, as illlustrated in Figure 3. It can be expressed as:

$$\boldsymbol{f}_{\mathrm{vm},i} = \frac{\rho_f V_p}{2} \frac{\partial}{\partial t} \left(\boldsymbol{u} - \boldsymbol{v}_i \right) \tag{16}$$

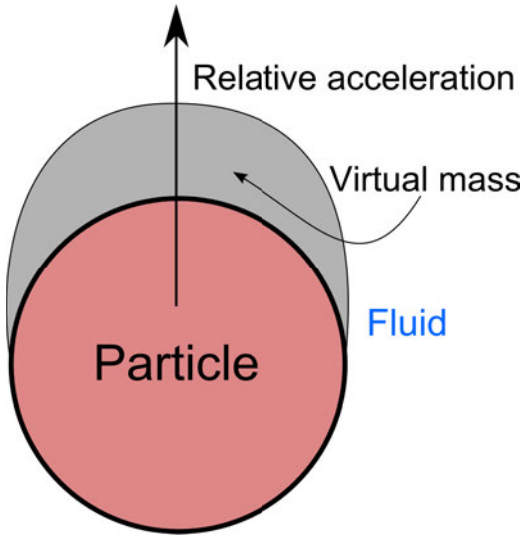

Figure 3: Scheme of the virtual mass force, adapted from Crowe *et al.* [73]

Although negligible if the suspending fluid is air, this force is of greater importnace in the case of a liquid. However, as noted by Arolla and Desjardins [76], no expression has been developed for this force in the case of non-vanishing Re_p or non-dilute particle concentrations. Consequently, the contribution of this force to the solid-liquid dynamics was not taken into account in our model.

We note that authors such as Derksen [43] have implemented the virtual mass by

adding $\pi\rho_f \frac{d_p^3}{12}$ to the inertia of the particles on the left side of Eq. (2). We believe this is not an adequate implementation of this force as it does not take into account the time derivative of the fluid velocity and is not two-way coupled.

Work is definitely required to design a virtual mass expression that is valid for a wide range of solids concentrations and particle Reynolds numbers.

3.5. Calculation of the void fraction and momentum exchange term for the liquid phase flow (CFD)

In this work, two-way coupling is carried out by projecting the volume of the particles and the solid-fluid forces onto the CFD mesh in order to calculate the void fraction ϵ_f and the momentum exchange term $\boldsymbol{F}_{pf}$. Ideally, the projection method should minimize the occurence of discontinuities for ϵ_f and $\boldsymbol{F}_{pf}$ to prevent instabilities [77, 78].

In the present work, we use the so-called divided approach of the CFDEM framework. It subdivides the projected particle into 27 regions of equal volumes, each of which is represented by a point and a fraction ($\frac{1}{27}$) of the particle volume. These points are located on the mesh to calculate the void fraction and the momentum exchange term. This approach has the significant advantage of being mass conservative while smoothing the void fraction and the momentum exchange term [25].

4. Determination of the just-suspended speed and the fraction of suspended particles

In this section, the methods used in the current work to evaluate the just-suspended speed and the fraction of suspended particles by means of a Euler-Lagrange model are presented. Two novel methods are introduced. The first one, the so-called Lagrangian suspended fraction analysis technique (in two variants: LSFA-$\Delta \boldsymbol{x}$ and LSFA-Δz), is based on the analysis of the motion of each individual particle. The second one, dubbed the decorrelated fraction analysis (DFA) technique, makes use of the mixing index introduced by Doucet *et al.* [79] to quantify the degree of decorrelation between the particles with respect to time. The pressure gauge technique, as proposed by Micale *et al.* [23], is first presented in detail since it is used extensively in this work. Other methods from the literature are also briefly introduced. A thorough review of the methods available to measure N_{js} can be found in Tamburini *et al.* [36] and Kasat and Prandit [5].

4.1. Pressure gauge technique

The pressure gauge technique measures the fraction of suspended particles by correlating it with the increase of the static pressure at the bottom of the vessel [22, 23].

More precisely, as the particle bed is eroded and the suspension process begins, the apparent density of the liquid increases as particles are dragged by the liquid, which results in an increase of the hydrostatic pressure at the bottom of the tank. Once all

the particles have been suspended, the apparent density and the hydrostatic pressure level off to a constant value. Consequently, the fraction of suspended particles can be obtained from the increase of the hydrostatic pressure (ΔP_{susp}). Given that the probe measures the total pressure at the bottom of the tank, and the increase of the impeller velocity increases the dynamic component of this pressure, it is necessary to extract the static pressure from this total pressure. By fitting a second order polynomial curve ($\Delta P = aN^2 + b$) on the pressure measurement past the inflexion point on the total pressure curve, it is possible to subtract the dynamic component of the pressure from the total pressure and thus deduce the variation of the hydrostatic pressure (ΔP_{susp}). The fraction of suspended solids (X_{susp}) can also be obtained straightforwardly from the variation of the hydrostatic pressure. The reader is referred to the work of Micale *et al.* [23] or to our recent work [7, 25] for more details.

This measurement method can be easily applied to CFD-DEM simulation results. Indeed, we showed that, in the laminar and transitional regimes, the total pressure at the bottom of the tank can be obtained from unresolved CFD-DEM simulations by averaging the pressure within a ring at the bottom of the vessel [25]. Our results revealed that the fraction of suspended solids predicted with the same CFD-DEM model used in the current work compared well to our experimental data [7].

4.2. Lagrangian suspended fraction analysis (LSFA) technique

It is often mentioned in the literature (*e.g.* [36]) that Euler-Lagrange simulations of solid-liquid mixing should allow for a natural interpretation of Zwietering criterion. We recall that, according to Zwietering [4], N_{js} corresponds to the impeller speed at which no particle remains motionless at the bottom for more than 1 or2 s.

However, translating this relatively heuristic definition to an objective criterion based on a Lagrangian description of the particles is not straightforward. This criterion consists of observing each particle at the bottom of the tank - that is a particle in contact with either the tank bottom or the particle bed - within a time window (Δt_{js}), and considering that a particle is suspended if it has moved a certain distance either in any direction ($\Delta \boldsymbol{x}_{js}$) or along the axial direction (Δz_{js}) of the tank. The use of either $\Delta \boldsymbol{x}_{js}$ (LSFA-$\Delta \boldsymbol{x}$) or Δz_{js} (LSFA-Δz), the latter being a harsher criterion, is debatable. However, $\Delta \boldsymbol{x}_{js}$ appears to be closer to industrial needs. For instance, a particle can remain very close to the vessel bottom, but circulate and be in contact with constantly renewed fluid, thus allowing efficient mass transfer. Both approaches will be considered in the present work and their efficiencies will be compared. Figure 4 illustrates the different cases that may occur over a time duration Δt_{js} with the LSFA-Δz approach. The LSFA-$\Delta \boldsymbol{x}$ approach is identical with the exception that the displacement is in all directions ($\mathbb{R}^3$) instead of solely along the $\boldsymbol{z}$ axis.

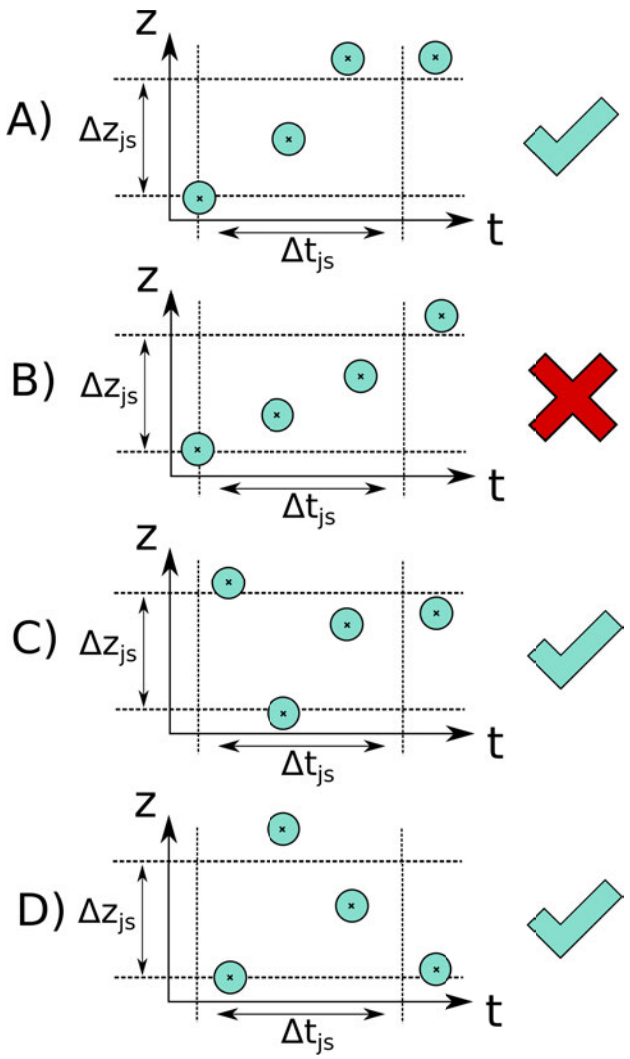

Figure 4: Scenarios that may occur over a time duration Δt_{js} with the Lagrangian suspended fraction analysis technique: (A) the particle is sufficiently lifted up from the bottom, (B) the particle is unsufficiently lifted up from the bottom, (C) the particle settles during the time window and is displaced unsufficiently, and (D) the particle is first lifted up and then settles to the tank bottom

Defining values for Δt_{js} and Δz_{js} or $\Delta \boldsymbol{x}_{js}$ is not trivial since multiple time scales and length scales co-exist within the stirred tank. On the basis of Zwietering's original definition, it seems appropriate to define $\Delta t_{js} \in [0.5, 3]$. Furthermore, since the suspension process is intuitively linked to the diameter of the particles, Δz_{js} (or $\Delta \boldsymbol{x}_{js}$) should be defined accordingly; a possible choice is then $\Delta z_{js} = \kappa d_p$, with $\kappa \in [0.5, 5]$. This will be investigated in the present work.

4.3. Decorrelated fraction analysis (DFA) technique

The decorrelated fraction analysis technique uses the weak mixing index introduced by Doucet *et al.* [79] to measure the degree of suspension of the particles.

This index quantifies the efficiency of mixing operations using the Lagrangian trajectories of particles (or massless tracers). It is based on a principal component analysis (PCA) [80], which measures the correlation between the position of all particles at time t ($\boldsymbol{x}_t$) and their position at time t_0 ($\boldsymbol{x}_{t_0}$) (weak index). The position can be supplemented by particles properties (*e.g.* size, shape, density), leading to the strong mixing index [79].

The PCA results in the solution of an eigenvalue problem for a $d \times d$ system of equations, where d is the number of dimensions considered. The mixing index is calculated by normalizing the largest eigenvalue ($\lambda_k = \max(\lambda_j)$, with $j \in [1, d]$) with respect to its initial value. If this eigenvalue decreases to a constant that is not asymptotically zero, the system is considered to be poorly mixed along the direction corresponding to the

eigenvector associated with λ_k. However, this condition is a necessary but not sufficient condition for a system to be well-mixed. In other words, an asymptotically decreasing mixing index ($\lambda_k \to 0$) does not necessary imply a well-mixed system, whereas a non-zero value ($\lambda_k \to C > 0$) reveals that the system does not mix well, depending on how C is close to zero. The reader is referred to [81] for more details.

The mixing index can be used to measure the degree of suspension in stirred tanks. At time $t_0 + \Delta t_{js}$, only a particle that was already in a suspended state or that was suspended during this time interval can have its position decorrelated from that at time t_0. Otherwise, if a particle remains unsuspended, then its actual position still correlates to its initial one. The value of the normalized eigenvalue (λ_k) is thus linked to the fraction of unsuspended particles, assuming that once a particle gets suspended, it is also considered distributed or mixed. This is a plausible hypothesis in the early turbulent regime due to the presence of unsteady turbulent structures. The mixing index analysis in this work is carried out in cylindrical coordinates ($[\boldsymbol{e}_r, \boldsymbol{e}_\theta, \boldsymbol{e}_z]$) since this is the most appropriate coordinate system to represent the motion of particles in a stirred tank.

4.4. Tangent-intersection analysis (TIA) technique

The tangent-intersection analysis (TIA) technique [34] is based on the evaluation of the average solids concentration on a plane at a height 1 mm above the tank bottom. The mean solids concentration is plotted as a function of the impeller speed and two tangents

lines to the curve are drawn where the slope is minimum and maximum. N_{js} is then defined as the speed at which these two lines intercept.

4.5. Local particle concentration technique

In this method introduced by Bourne and Sharma [82], the particle concentration is measured as a function of the impeller speed in a zone below the impeller but above the top of the bed of particles. This fraction, initially small, increases with the impeller speed as the number of suspended particle increases. Above a certain impeller speed, the particles at the vessel bottom get all suspended. Past this point, further increasing the impeller speed only increases the homogeneity of the suspension, which results in a decrease of the particle concentration in the measurement zone. Bourne and Sharma [82] define the just-suspended speed N_{js} as the impeller speed at which this change occurs.

4.6. Transient solids concentration technique

Kee and Tan [83] monitored the solids volume fraction in the cells in contact with the vessel bottom and proposed to identify N_{js} as the impeller speed at which the solids concentration at all points above the vessel bottom reaches a steady-state value smaller than 50% of the initial packed volume fraction ($\epsilon_{p,m}$). According to these authors, if all cells above the impeller bottom reach such a constant steady-state value, it is reasonable to consider that the quantity of solids circulating in the tank does not fluctuate with time.

Furthermore, if particles accumulate at the bottom of the tank, those regions will have a volume fraction larger than $0.5\epsilon_{p,m}$, thus violating the criterion.

4.7. Power number technique

This method is based on the analysis of the variation of the power number ($N_p = \frac{P}{\rho_f D^5 N^3}$, with P the power consumption) with the increase of the impeller speed. Different authors have observed varying trends for N_p as N increases, as reviewed by Tamburini *et al.* [24]. In particular, Rewatkar *et al.* [39] noted a decrease of N_p when N is below N_{js}, which they related to the reorganization of the particles in the bed. Then, they observed a sudden increase of N_p due to the increase of the apparent density caused by the suspended particles, until a constant N_p was reached. Other authors, such as Rahagava Rao *et al.* [40] and Michelleti [84] obtained a monotonically increasing value of N_p with N until a plateau is reached. Rahagava Rao *et al.* [40] and Rewatkar [39] proposed to define N_{js} as the speed at which this plateau was attained, since, above this point, the apparent density of the suspension remains constant.

5. Methodology

In this section, the methodology used for both experiments and simulations are described in detail.

5.1. Experimental set-up for the PGT measurements

The experimental rig used is presented in Figure 1 of Section 2. In this rig, the pressure is measured by means of a Freescale sensor (MPX5010DP), with a precision of 5%, connected to a tube which is in turn connected to a hole at the bottom of the tank. This allows for the recording of the evolution of the pressure with time. The end of the tube at the bottom of the tank is fitted out with a thin screen, which prevents clogging and dims the effects of the variation of the dynamic pressure due to turbulent fluctuations, thereby reducing the noise level in the total pressure measurements. The experiments were carried out four times in order to assess the repeatability and estimate the errors on the measurements by means of confidence intervals. One seperate experiment where the impeller speed was ramped up and down revealed no hysteresis in the measurements.

5.2. Simulation set-up

Simulations were carried out using the unresolved CFD-DEM model presented in Section 3. The model parameters used are given in Table 4. The same mechanical properties are given to both the walls and the particles. These mechanical properties were taken from the work of Di Renzo and Di Maio [85], Di Renzo *et al.* [86] and Shao *et al.* [44] for glass beads suspended in a liquid. To reproduce the size distribution of the particles that were used experimentally, 10 different diameters d_p were considered ranging from 2.66 to 3.5 mm. A total of 130 000 particles were required to reach the mass fraction

of 10%.

The fluid considered is a glucose solution of viscosity of 0.0516 Pa.s, as discussed in Section 2. This fluid, of viscosity higher than that of water, was chosen to preclude the need for a very fine mesh. It also allows for an easier resolution of the large turbulent scales.

The simulations were all transient. Initially, a static bed of particles was generated at the bottom of the vessel by sedimentation of the particles by means of DEM simulations. It was found that changing the random seed used for the insertion of particles did not lead to significant change in the results. This was assessed by carrying out three different simulations at $N = 100$RPM, $N = 300$RPM and $N = 500$RPM.

The simulations were carried out for a duration that varied depending on the impeller speed. For $N < 225$ RPM, 25 s of flow were obtained, whereas 15 s and 12 s of flow were obtained for $N \in [225, 450]$ and $N > 450$, respectively. For all impeller speed, a constant mean value of the pressure was obtained for at least 6 s, indicating that the system had reached steady-state.

The power consumption was calculated using the torque on the impeller, which was extracted by integrating the forcing term of the PISO-IB method [51]. The total pressure at the bottom of the tank was calculated by integrating the pressure in a circular region mimicking the pressure sensor position. We refer to our previous work for more details

Table 4: Parameters for the solid-liquid mixing simulations

Symbol	**Name**	**Value**
Y	Young's modulus	100 MPa
e_r	Coefficient of restitution	0.9
ν	Poisson ratio	0.25
μ_f	Coefficient of friction	0.3
μ_r	Rolling friction	0.1
Δt_{DEM}	DEM time step	5×10^{-6} s
$\Delta t_{CFD,N\leq 225}$	CFD time step	2×10^{-4} s
$\Delta t_{CFD,N\in[250,450]}$	CFD time step	1×10^{-4} s
$\Delta t_{CFD,N>450}$	CFD time step	5×10^{-5} s
$\Delta t_{c,N\leq 225}$	Coupling time step	2×10^{-4} s
$\Delta t_{c,N\in[250,450]}$	Coupling time step	1×10^{-4} s
$\Delta t_{c,N>450}$	Coupling time step	5×10^{-5} s

on this procedure [25].

460 *5.2.1. Mesh design and sensitivity analysis*

The background hexahedral mesh generated for the CFD part consisted of 33x136x90 (r,θ,z) cells with local mesh refinement in the swept volume of the impeller and close to the free surface, the tank walls and the baffles, for a total of 1.2M fluid cells. The maximal Courant-Friedrichs-Lewy condition for all simulations was below 0.70, which means stable solutions were obtained. The time step for the DEM particles was below 15% of the characteristic time of Rayleigh waves ensuring the stability of DEM results. We recall the expression for the characteristic time of the Rayleigh waves (Δt_{Ra}) [48] :

$$\Delta t_{Ra} = \frac{\Pi}{2} d_p \sqrt{\frac{\rho_p}{G}} \left(\frac{1}{0.1631\nu + 0.8766} \right) \tag{17}$$

It was found that mesh refinement past this level did not lead to measurable changes in the torque ($< 1\%$) for single phase flows at the maximal impeller speed considered in this work (900 RPM). Mesh independence was observed with less cells when the impeller speed was lower.

To perform a mesh sensitivity analysis for the unresolved CFD-DEM simulations, a coarser mesh, with 0.95M cells, and a finer mesh, with 1.5M cells, were considered in addition to the original mesh of 1.2M cells. The pressure at the bottom of the tank, a very sensitive variable that is affected by the local flow as well as the suspension, was measured at the bottom of the vessel. This analysis was carried out for impeller speeds of 100, 300, 500, 700 and 900 RPM. For $N = 100$ and $N = 300$, the relative error on the pressure for the coarse and original meshes was below 1% with respect to the finer mesh. For $N > 300$, the coarser mesh error with respect to the finer mesh was 6% for impellers speeds of 500 and 900. However, the differences in the pressure results between the original and the finer meshes were lower than 1% for all impeller speeds.

The simulations were carried out on the Colosse cluster of Calcul Québec. Each simulation used 4 Intel Xeon X5560 quad-core 2.8 GHz processors distributed on two nodes (total of 16 cores) with 12 GB of memory available for each processor (48 GB total). The memory required for the simulations was less than 10GB. The simulations required from 2 to 3 weeks of computational time depending on the time steps used.

6. Results and discussion

In this section, the flow patterns and the distribution of particles obtained with the LES-based unresolved CFD-DEM model described in Section 3 are discussed. Then, the model is validated by comparing the fraction of suspended particles measured in our lab using the pressure gauge technique (PGT) to the results obtained with the unresolved CFD-DEM model. More precisely, the results from the Lagrangian suspended fraction analysis (LSFA-$\Delta \boldsymbol{x}$ and LSFA-Δz) and the decorrelated fraction analysis (DFA) techniques are compared to the PGT data. Finally, the potential of all methods described in Section 4 to predict N_{js} (and N_{ss}) with respect to Zwietering correlation is assessed.

6.1. Flow patterns and solids distribution

The flow profiles were phase averaged over a period of at least 6 s for a relatively large number of impeller revolutions (10 at the lowest impeller speed investigated (100 RPM) and 90 at 900 RPM) on two planes :

- $\boldsymbol{P}_y$: normal vector $[-0.05\ 1\ 0]^T$ and centered at (0 0 0). This plane is adjacent to the baffles;
- $\boldsymbol{P}_{xy}$: normal vector $[1\ 1\ 0]^T$ and centered at (0 0 0)

These planes are illustrated in Figure 5.

Phase averages where carried out over various periods (for instance, from 3 s to 6 s for $N \geq 500$) and it was found that the phase averaged velocity and void fraction were unchanged for averaging periods larger than 4s.

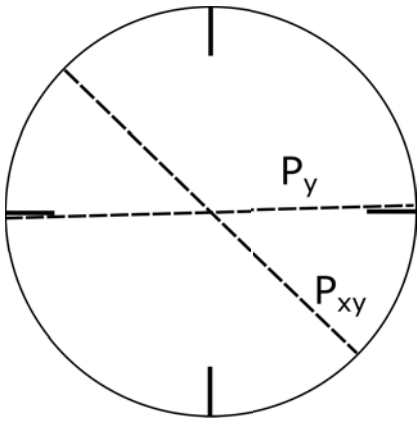

Figure 5: Illustration of the planes on which the phase averaging was carried out.

Figure 6 shows the phase averaged void fraction ϵ_f at 500 RPM, a speed at which the experiments and the PGT results (shown in Figure 11 and discussed later) indicate a fully suspended state.

Zones of higher concentration can be identified at the wall-bottom junction. Their locations coincide with the zones where the last particles were observed to get suspended in the experiments.

Figure 7 presents the void fraction ϵ_f at $N = 900$ RPM, the maximum impeller speed investigated in the present work. It can be seen that even at such a high impeller speed, the particle concentration is not homogeneous in the tank. More precisely, it is higher

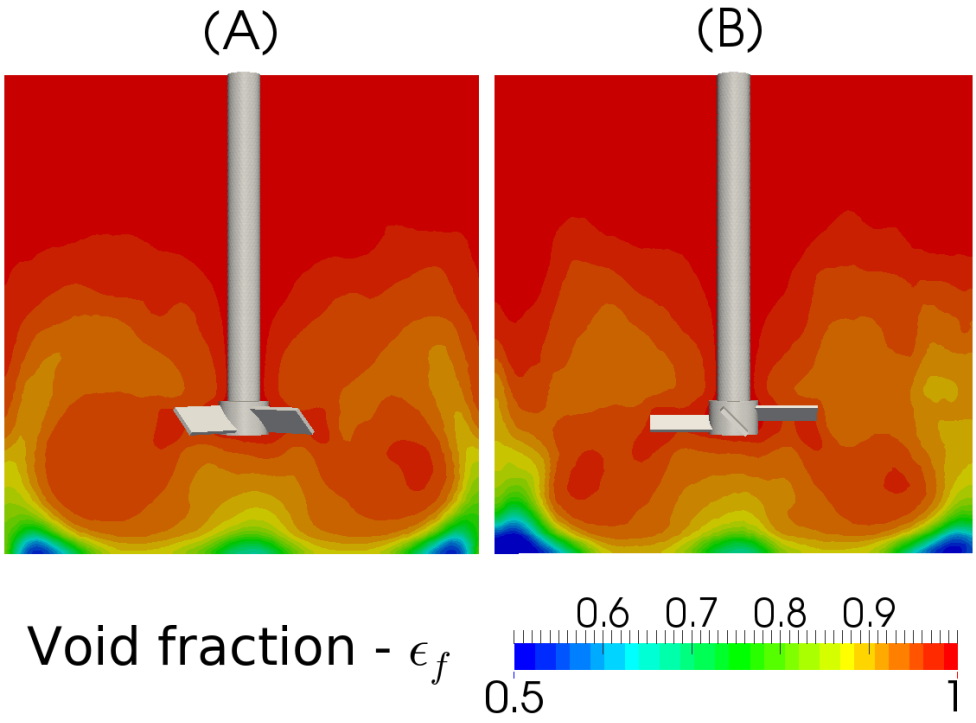

Figure 6: Phase averaged void fraction (ϵ_f) for $N = 500$RPM on the (A) $\boldsymbol{P}_{xy}$ and (B) $\boldsymbol{P}_y$ planes.

in the near-baffle region where the particles are dragged upward along the tank wall. A toroid can also be observed below the impeller, within which the particle concentration approaches zero. Albeit slightly visible at $N = 500RPM$ (Figure 6), this structure is enhanced significantly at $N = 900$ RPM (Figure 7). We believe that this phenomenon is due to the presence of a high-vorticity toroid-like structure, which expels the particles.

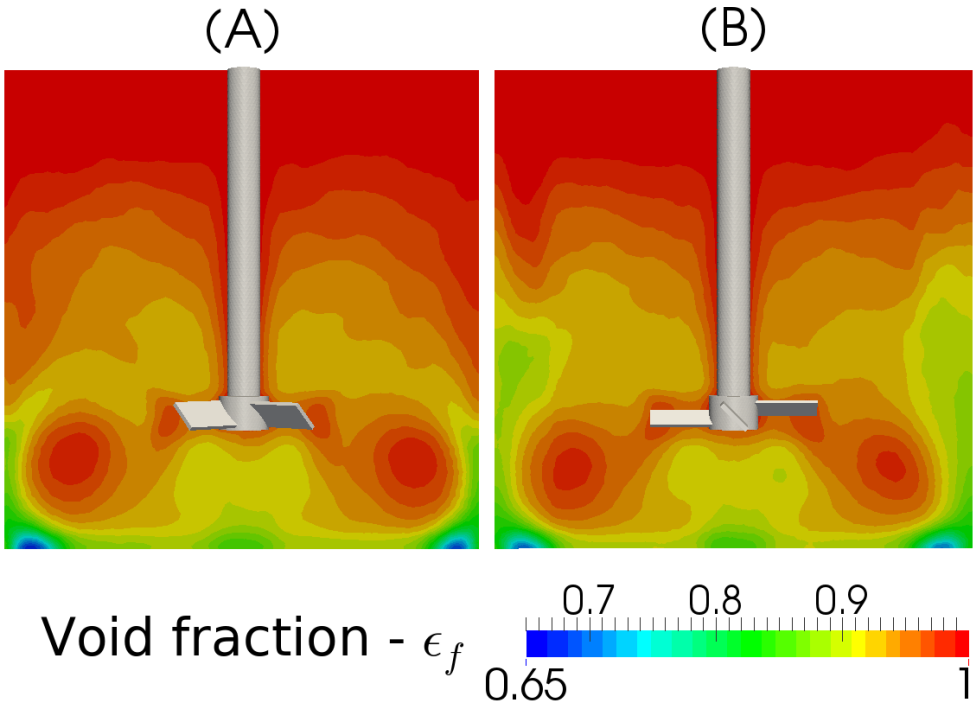

Figure 7: Phase averaged void fraction (ϵ_f) for $N = 900$RPM on the (A) $\boldsymbol{P}_{xy}$ and (B) $\boldsymbol{P}_y$ planes.

The contours in Figure 8 show the phase averaged void fraction in the $\boldsymbol{P}_y$ plane at impeller speeds of 100 RPM, 200 RPM, 300 RPM, while the velocity magnitude profiles

at the same impeller speeds are presented in Figure 9. At low speed ($N = 100$ RPM), the kinetic energy is insufficient to erode the particle bed. For the impeller, the particles at the bottom of the tank are like a rigid volume, which leads to more radial flow patterns where the magnitude of the velocity is only significant above the bed. Increasing the impeller speed eventually leads to the deformation of the particle bed, in reaction to the fluid jet induced by the PBT. The motion of the particles in turn alters the fluid flow patterns, the magnitude of which become more and more significant at the bottom of the impeller. Consequently, the discharge of the impeller becomes more and more axial as the impeller speed is increased and the particle bed is eroded. At $N = 300$ RPM, the particles at the center of the vessel are all in motion, since the volume fraction of fluid (ϵ_f) is way above the fluid fraction at the maximal solids packing ($\epsilon_f = 1 - \epsilon_{p,m} = 0.36$), and the flow patterns are fully axial. The unsuspended particles are mainly located at the wall-bottom junction. At higher impeller speed, the velocity profile is not altered significantly and remains principally axial.

It is interesting to observe where the relative velocity between the particles and the fluid (characterized by the particle Reynolds number $Re_p = \frac{\rho_f d_p |\bar{\boldsymbol{u}} - \boldsymbol{v}|}{\mu}$) is significant. Figure 10 shows the value of Re_p for $N = 900$ RPM in the $\boldsymbol{P}_{xy}$ and $\boldsymbol{P}_y$ planes, which is the velocity at which the maximal values of Re_p were observed. Re_p appears to be relatively large in small regions close to the impeller, the baffles and the tank bottom.

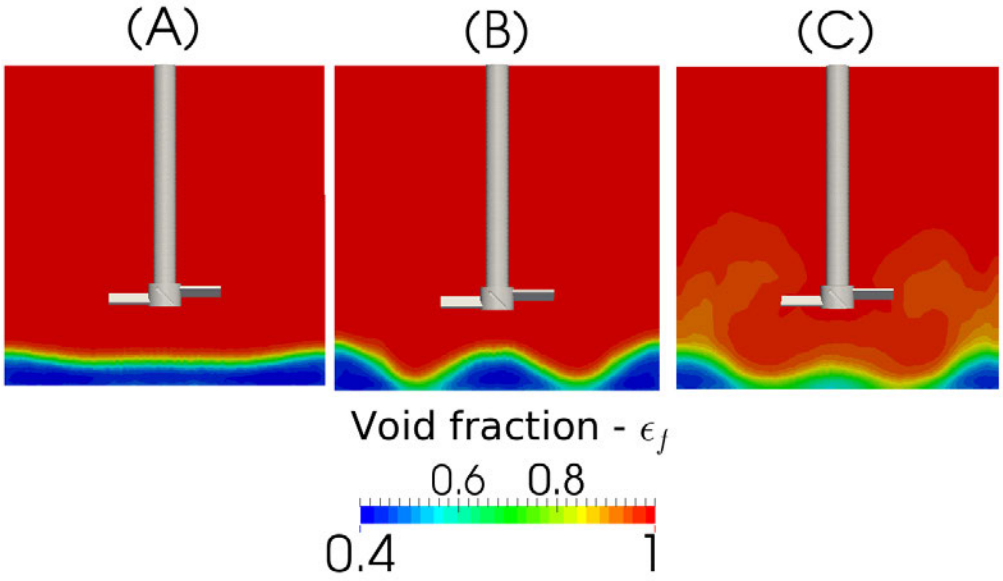

Figure 8: Phase averaged void fraction (ϵ_f) on the $\boldsymbol{P}_y$ plane for (A) $N = 100$ RPM, (B) $N = 200$ RPM and (C) $N = 300$ RPM.

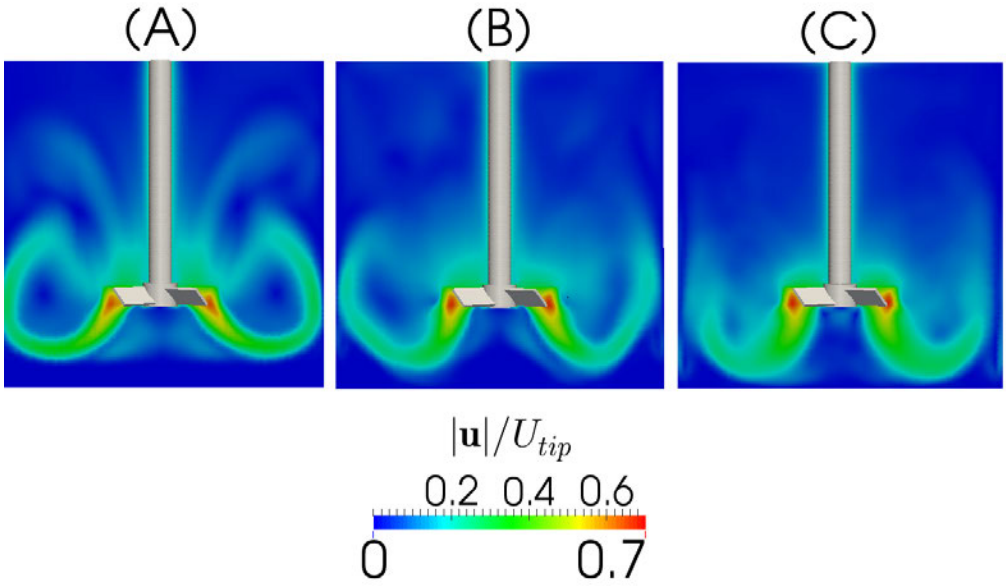

Figure 9: Phase averaged velocity magnitude ($|\bar{\boldsymbol{u}}|$) on the $\boldsymbol{P}_y$ plane for (A) $N = 100$ RPM, (B) $N = 200$ RPM and (C) $N = 300$ RPM.

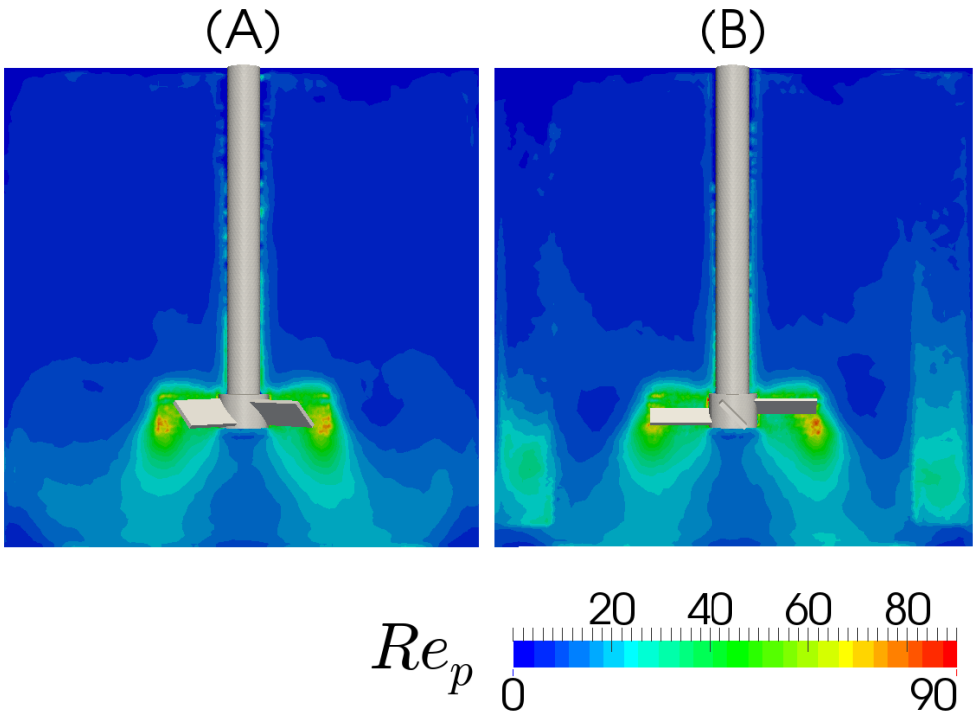

Figure 10: Phase averaged Re_p values for $N = 900$ RPM on the (A) $\boldsymbol{P}_{xy}$ and (B) $\boldsymbol{P}_y$ planes. The Re_p value for a freely sedimenting particle is 5.7 for this system.

Elsewhere, the positive values of Re_p are only due to the action of gravity that pulls the particles down. It can be concluded that, on average, slip between the liquid and solid phases only occurs due to the components of the geometry, with the impeller and the baffles playing the most important role.

6.2. Suspension curves and just-suspended speed

In this section, the CFD-DEM model is validated for the fraction of suspended solids. Then, various ways to obtain suspension curves and the just-suspended speed are investigated. An extensive comparison between all these techniques is carried out.

6.2.1. Pressure gauge technique : experimental and numerical investigation

The graph in Figure 11 shows the fraction of suspended particles as a function of the impeller speed for both the experiments and the simulations. The error bars represent a 95% confidence interval established with a two-sided Student distribution. Due to the limited number of repetitions of each experiment (4 times), these errors are 2.78 times the standard deviation, which explains the relatively large error bars in Figure 11.

It can be seen that the CFD-DEM model is able to predict the speed at which full suspension is achieved with remarkable accuracy. However, at low speed ($N \leq 200$ RPM), the model appears to underestimate the fraction of suspended particles by up to 15%. All the data with the exception of those at $N = 175$ RPM are within the error bars. However, it must be noted that these error bars, representing 95% confidence intervals obtained with 4 experiments, are quite large for impeller speeds at which only partially suspended states are obtained. Overall, we note that the transition from a fully sedimented state to a fully suspended state is sharper for the numerical model than what is measured experimentally. This difference could be due to unresolved hydrodynamic effects related

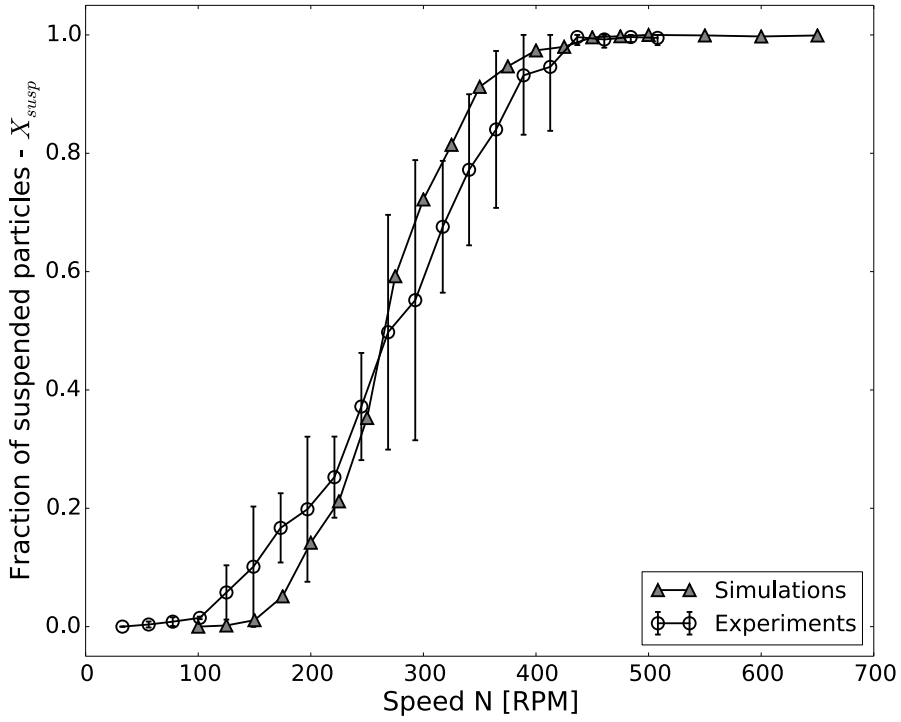

Figure 11: Comparison of the experimental and numerical suspension curves after application of the PGT procedure and the removal of the dynamic pressure component. The error bars represent a 95% confidence interval.

to the use of the VANS equations and the LES sub-grid closure model (see Section 3.2).

6.2.2. Lagrangian suspended fraction analysis technique

As described in Section 4, translating Zwietering criterion to an objective metric that can be reproduced numerically is not straightforward, mainly due to the need of defining a time observation window (Δt_{js}) as well as a minimal displacement ($\Delta \boldsymbol{x}_{js}$) or ($\Delta z_{js}$) for a particle to be considered suspended. The graph in Figure 12 contains typical suspension curves obtained via $LSFA - \Delta \boldsymbol{x}$ at steady-state using observation windows (Δt_{js}) up to 3 s, for various impeller speeds and a minimal displacement of $\Delta \boldsymbol{x}_{js} = d_p$.

For all values of N, the fraction of unsuspended particles initially tends to change abruptly, then decreases monotonically with time. These results also show that the fraction of suspended solids defined through this approach is sensitive to the choice of Δt_{js}. In order to remain within the scope of Zwietering's original definition, the time window should be taken as $\Delta t_{js} \in [0.5, 3]$.

We notice that for large impeller speeds ($N \geq 600RPM$), all particles get suspended very quickly. For $N \geq 450$, more than 99.7% of the particles get suspended within 2 s. In other words, increasing N above 450 RPM has no real benifits. An analysis with LSFA-Δz (not shown here) leads to similar results, although with larger fractions of unsuspended solids for each impeller speed.

The graphs in Figure 13 and 14 show the evolution of the fraction of suspended

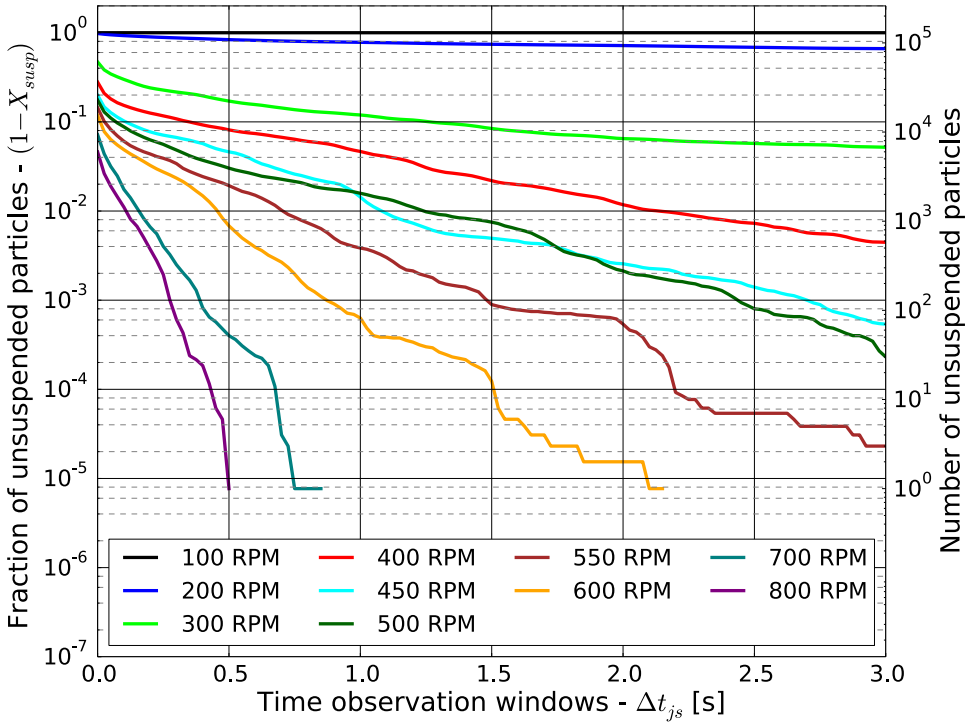

Figure 12: Evolution of the fraction of unsuspended particles calculated via LSFA-$\Delta \boldsymbol{x}$, as function of time, for various impeller speeds (N) and $\Delta \boldsymbol{x}_{js} = d_p$.

particles as a function of impeller speed N for various values of Δt_{js} and Δz_{js}, as evaluated with LSFA-$\Delta \boldsymbol{x}$ and LSFA-Δz, respectively.

We observe that all trends are similar and take the form of a Weibull (or S-shaped) function akin to what can be observed with the PGT results. Furthermore, for both LSFA-$\Delta \boldsymbol{x}$ and LSFA-Δz, increasing Δt_{js} increases X_{susp} whereas increasing $\Delta \boldsymbol{x}_{js}$ (or Δz_{js}) decreases X_{susp} without affecting the shape of the curve, except the sharpness of the transition and the speed at which the fully suspended plateau is reached. In particular, the effect of Δt_{js} is more pronounced than that of $\Delta \boldsymbol{x}_{js}$, indicating that once particles get suspended, they move significantly. All the curves converge to 1 for large enough values of N. Although the onset of the suspension is similar for LSFA-$\Delta \boldsymbol{x}$ and LSFA-Δz, the LSFA-Δz results seem to consistently underpredict the fraction of suspended particles for $N > 450$ RPM, when compared to the PGT results. In such a case the PGT and LSFA-$\Delta \boldsymbol{x}$ result indicate full suspension, at least for many values of Δt_{js} and Δx_{js} whereas the LSFA-Δz results tend to predict non-negligible amount of unsuspended particles. This is due to the presence of moving particles close to the vessel bottom, which are considered suspended by LSFA-$\Delta \boldsymbol{x}$ and the PGT, but which suffer from poor axial velocity and are not considered as suspended with LSFA-Δz. These particles are located close to the tank walls in the zones of higher concentration identified in Section 6.1.

The LSFA-$\Delta \boldsymbol{x}$ results agree more nicely with the PGT. The method can predict

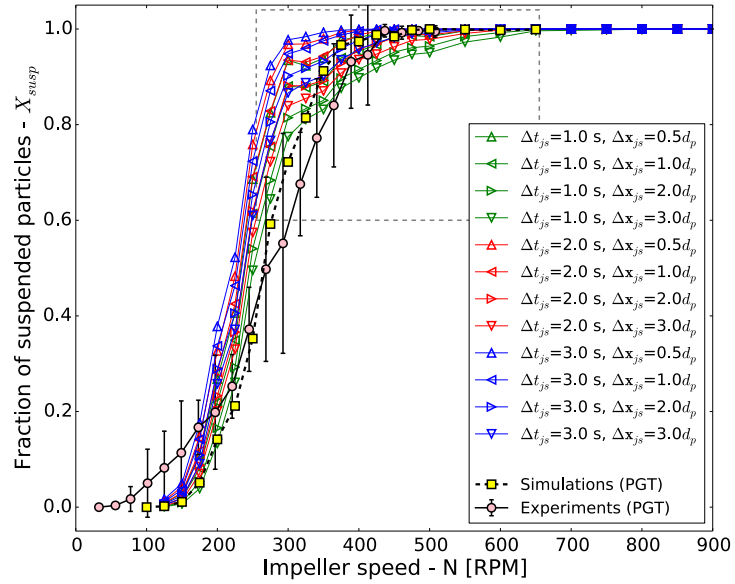

(A)

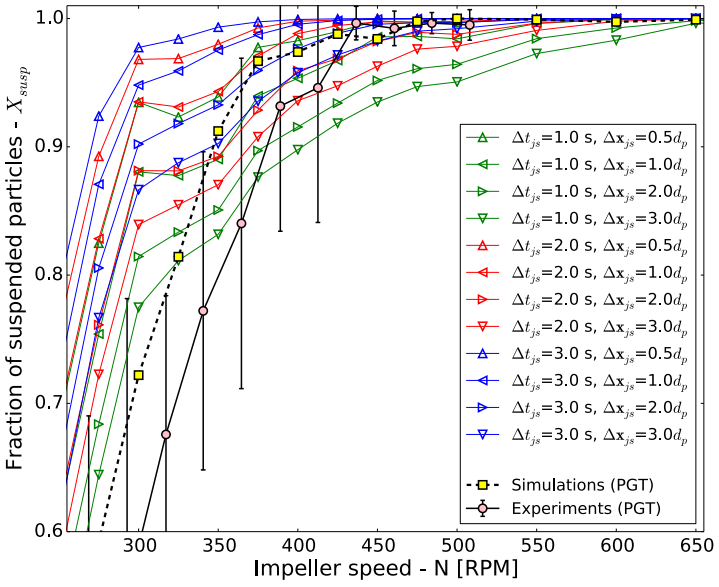

(B)

Figure 13: (A) Fraction of suspended particles measured by LSFA-$\Delta \boldsymbol{x}_{js}$ as a function of the impeller velocity (N), and comparison with the PGT results, and (B) zoom-in onto the area delimited by the grey rectangle in (A).

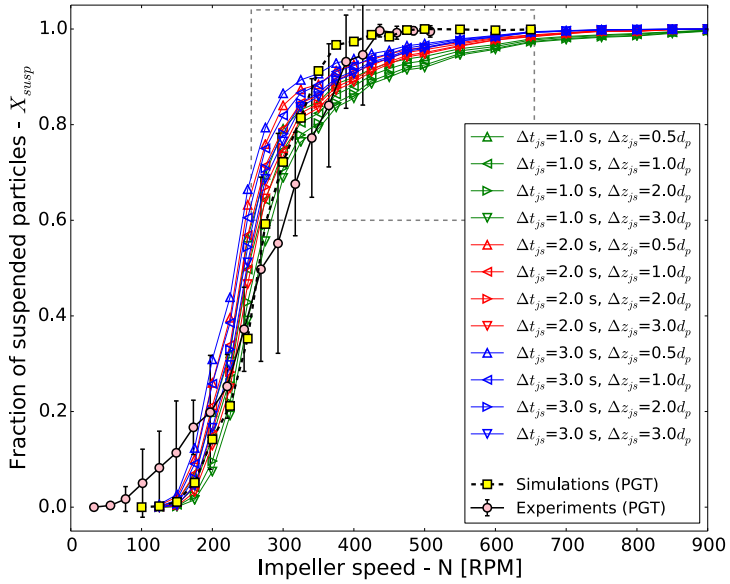

(A)

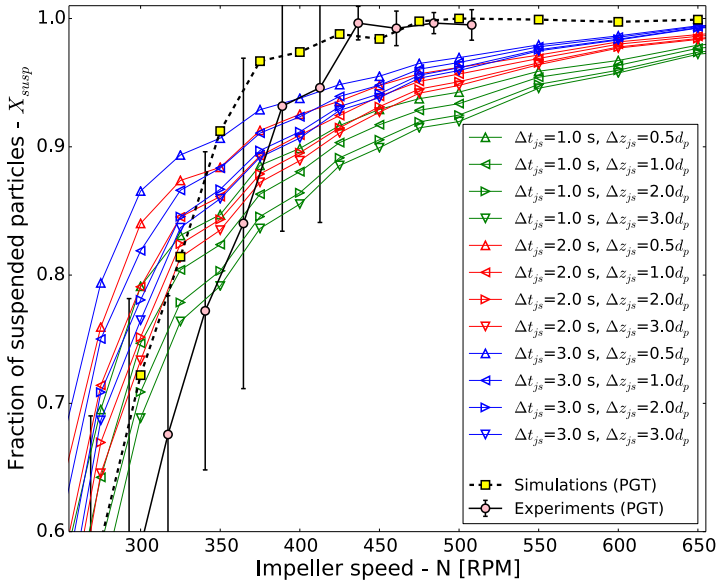

(B)

Figure 14: (A) Fraction of suspended particles measured by LSFA-$\Delta \boldsymbol{z}_{js}$ as a function of the impeller speed (N), and comparison with the PGT results, and (B) zoom-in onto the area delimited by the grey rectangle in (A).

adequately the fraction of suspended particles over a large range of impeller speeds and, although it seems to slightly overpredict X_{susp} for $N \in [200, 400]$, the results obtained with this technique remain within the confidence intervals.

6.2.3. Decorrelated fraction analysis

By comparison with the LSFA technique, the decorrelated fraction analysis (DFA) approach only requires the selection of an observation time Δt_{js}. The graph in Figure 15 compares the results obtained with the DFA to the PGT experimental and simulations.

For $\Delta t_{js} = 1$ s, the values of X_{susp} are below the PGT results for almost all impeller speeds. This is especially noticeable for $N > 425$, where X_{susp} reaches a plateau slightly below 1 even though a fully suspended state is observed at these speeds according to the PGT and LSFA-$\Delta \boldsymbol{x}$ methods (Figure 11 and 13). This means that the observation window is insufficiently long to allow for a full decorrelation of the positions of the particles even at speeds where adequate mixing occurs. The quality of the results improves for $\Delta t_{js} = 1.5$ s, but a plateau is again reached a little short of $X_{susp} = 1$. However, for $\Delta t_{js} \geq 2$ s, an excellent agreement is observed between the DFA and the PGT techniques, with the exception of a slight overprediction by the former for $N \in [300, 400]$ RPM. It is interesting to note that, for $\Delta t_{js} \geq 2$, the results become far less sensitive to the value of Δt_{js} as evidenced by the overlap in the $\Delta t_{js} \geq 2$ curves. Therefore, not only does this method not require the definition of a length, but there exists a time window above

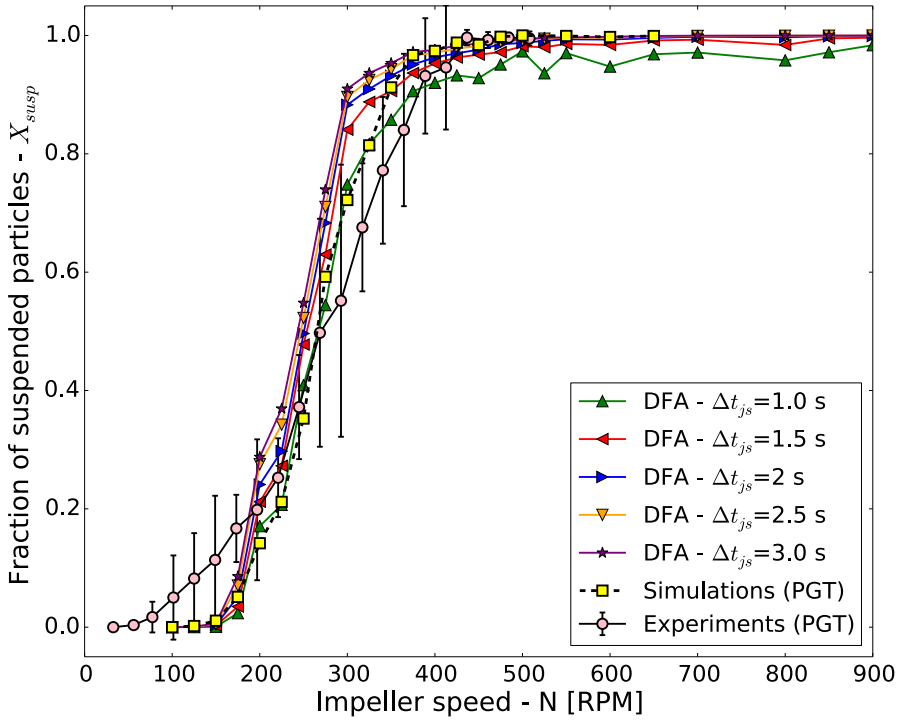

Figure 15: Fraction of suspended particles measured by DFA for various observation times (Δt_{js}), and comparison to PGT experimental and numerical results.

which the results converge to a constant value. Furthermore, it is interesting to note that this mixing index quantifies both the fraction of suspended solids and the efficiency with which these particles are mixed in the tank.

6.2.4. Tangent-intersection analysis technique

The graph in Figure 16 presents the results obtained by the tangent-intersection analysis (TIA) approach. A sharp transition in the void fraction ϵ_f with respect to the impeller speed can be observed starting from 175 RPM to 325 RPM. After 325 RPM, the void fraction slowly increases, but never reaches a constant plateau. Value of the average void fraction $\epsilon_f = 83\%$ at $N = 900$ RPM indicates the system never reaches a fully homogeneous state. Moreover, the N_{js} value obtained with this method, $N_{js,TIA} = 375$ is significantly below the values measured with the PGT, LSFA-$\Delta \boldsymbol{x}$ and DFA. This will be discussed in Section 6.2.8.

6.2.5. Power consumption technique

The graph in Figure 17 gives the power comsumption as a function of the impeller speed. Each value has been averaged over a period of 3 s. The power consumption can be observed to grow with N^3, indicating that the power number (N_p) is constant. The value of N_{js} cannot, in all likelihood, be determined from this curve.

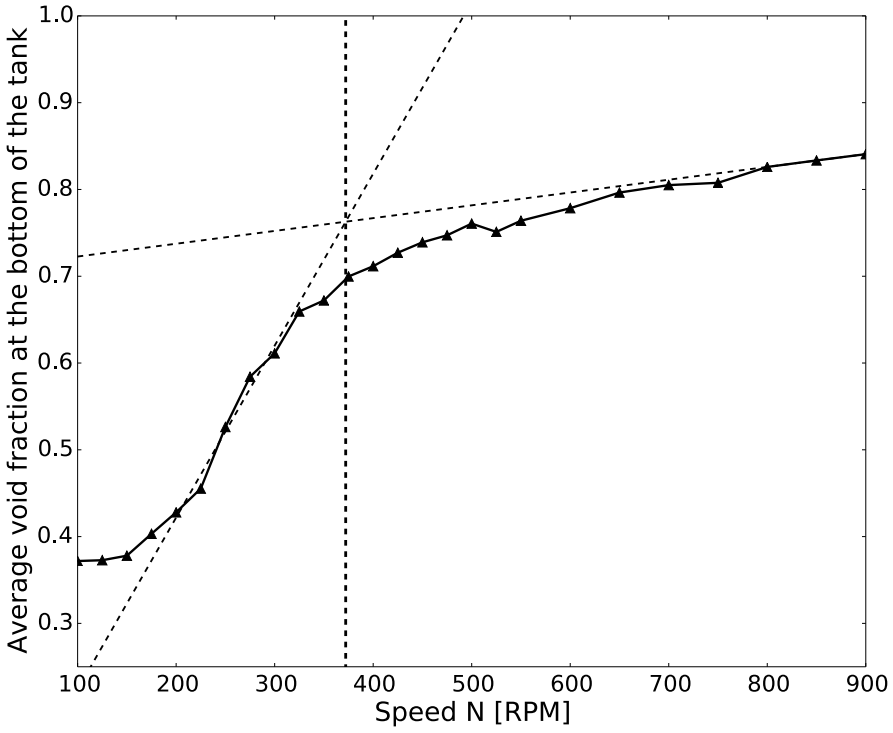

Figure 16: Evolution of the average void fraction 1 mm above the bottom of the tank and application of the tangent-intersection analysis approach.

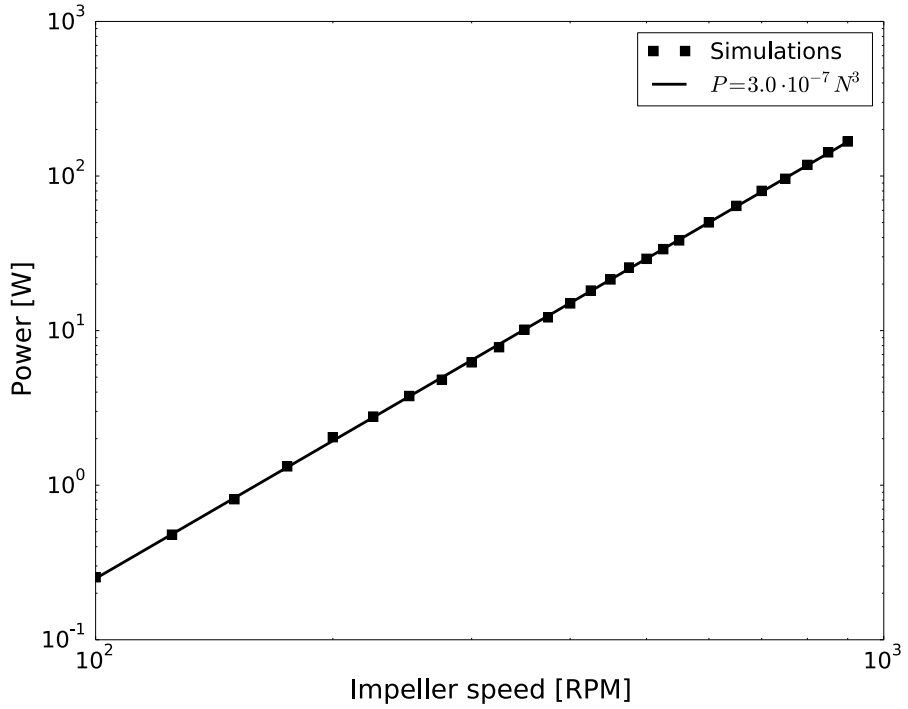

Figure 17: Power as a function of impeller speed

6.2.6. Local particle concentration technique

Phase averaged values of local particle concentrations were measured at three different positions on the phase averaged $\boldsymbol{P}_{xy}$ plane located below the impeller and 7 cm above the bottom of the vessel. These positions are illustrated at Figure 18

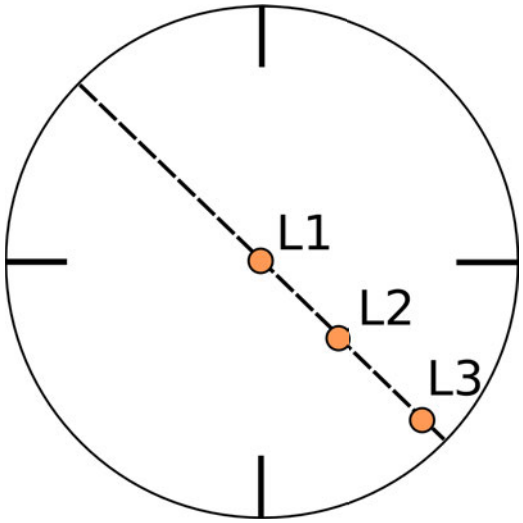

Figure 18: Positions of the measurement points for the local particle concentration technique

The graph in Figure 19 presents the values of the local void fraction at the three measurement locations with respect to the impeller speed. No clear trend from which N_{js} could be calculated can be observed. The failure of this approach to measure N_{js} for this system may be due to the fact that complete homogeneity is never reached. In other words, a plateau of the void fraction is never obtained and no value of N_{js} can therefore be deduced. Indeed, the value of the void fraction for the L1 and L3 measurements is

far below that at complete homogeneity which is $\epsilon_f = 0.949$, since the volume fraction of particles is 5.1% (see Table 1).

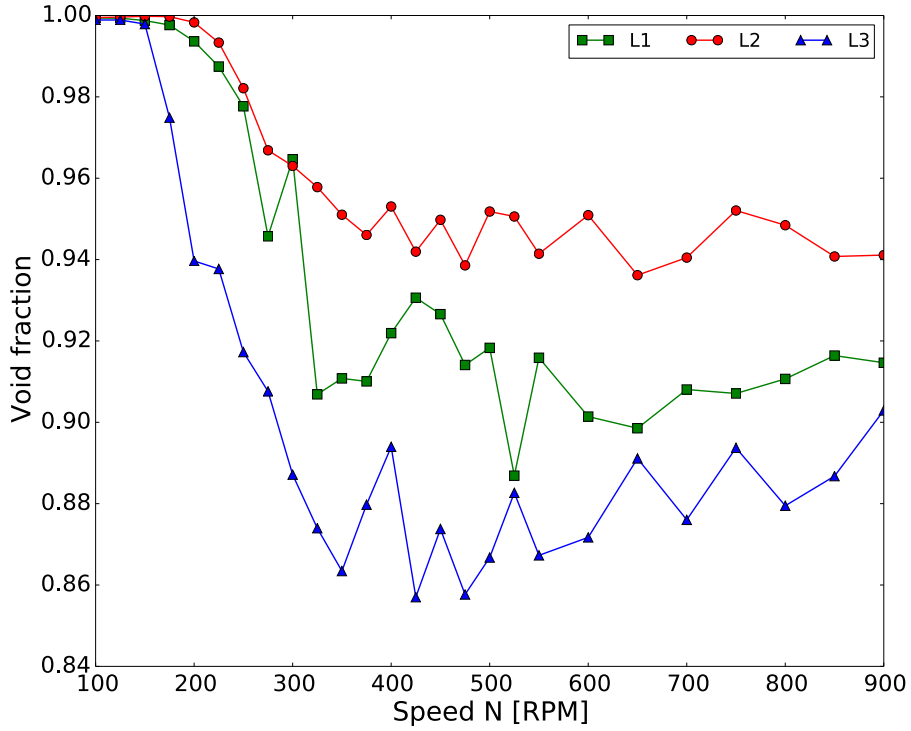

Figure 19: Values of the void fraction at the three measurement points with respect to the impeller speed.

6.2.7. Transient solid concentration technique

645 The graphs in Figure 20 display the phase averaged values of the void fraction on the $\boldsymbol{P}_{xy}$ plane for $N = 900$ RPM, 1 mm above the bottom of the tank. It can be seen that even at such a high impeller speed, where all particles are known to be suspended, there are

still zones where the solid concentration is more than half of the maximal packing fraction, that is $\epsilon_p = (1 - \epsilon_f) > \frac{\epsilon_{p,m}}{2}$ (as highlighted in blue in Figure 20 (B)). Consequently, no estimation of N_{js} can be made with this approach.

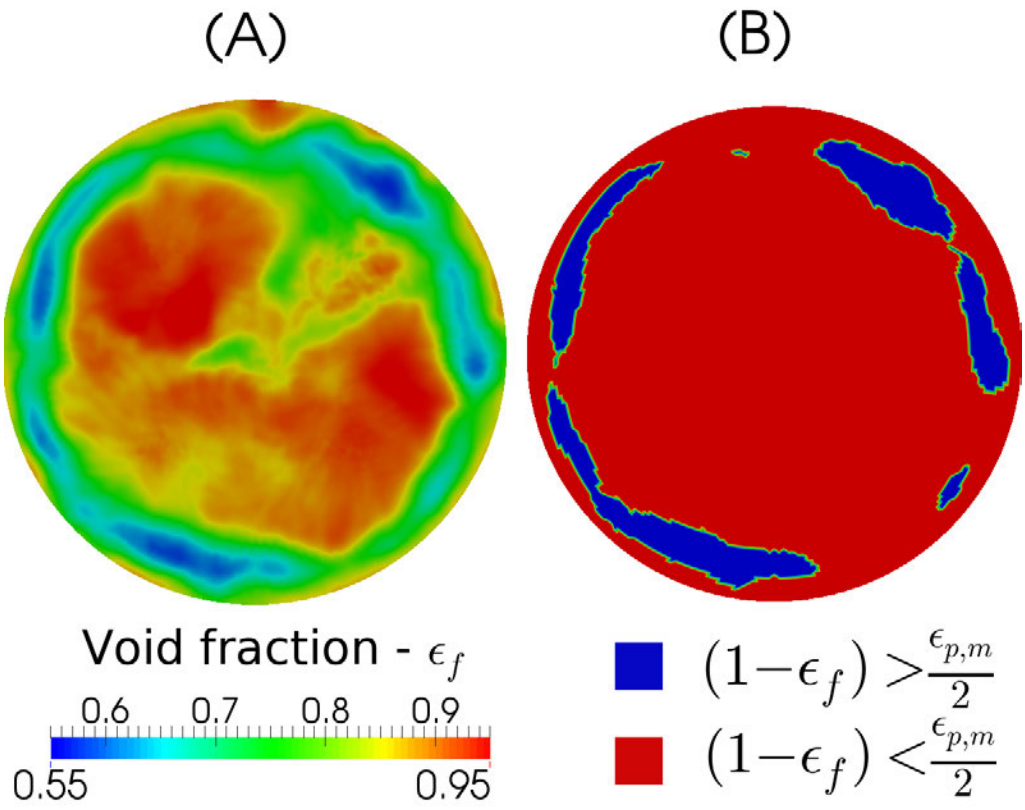

Figure 20: (A) void fraction on the $\boldsymbol{P}_{xy}$ plane 1 mm above the bottom fo the tank, and (B) zones where $(1 - \epsilon_f) > \frac{\epsilon_{p,m}}{2}$ at the bottom of the tank, for $N = 900$ RPM

6.2.8. Comparison of the strategies for the determination of N_{js}

As discussed in the previous sections, no clear estimation of N_{js} could be obtained by analyzing the power consumption (Section 6.2.5), local particle concentrations (Section 6.2.6) and transient solids concentrations (Section 6.2.7). This inability to predict N_{js} with these approaches could be due to their lack of generality, which makes them inadequate for systems involving relatively large particles in an early turbulent regime as in the current work ($d_p = 3$ mm, $Re < 6000$). In fact, there appears to be little physical foundation to support the tangent intersection (Section 6.2.4), transient solids concentration and local particle concentration approaches. Although more physically sound, the power consumption approach seems not sensitive enough to account for the suspension of the particles in the mixing system, which is most likely due to the fact that the impeller sees a fraction of particles that is too small to affect in an observable manner the power draw. The PGT, which is also based on the increase of the apparent density, does not suffer from such a drawback as it is a more global approach.

The PGT (Section 6.2.1), LSFA (Section 6.2.1) and DFA (Section 6.2.1) approaches were observed to be suitable for the evaluation of the fraction of suspended particles. In particular, they can serve to obtain the sufficiently suspended speed (N_{ss}), the latter being the speed at which $X_{susp} = 0.982$ [23] (see Section 1).

Table 5 compares the values of N_{ss} obtained via the PGT, LSFA, DFA techniques

to the values of N_{js} from the TIA technique and those predicted by the Zwietering correlation (with $S = 6.18$, a value taken from Table 6 of Lassaigne *et al.* [7]). The four rightmost columns of this table display the fraction of suspended particles X_{susp} at the impeller speed given in the corresponding rows. These values of X_{susp} were obtained by interpolating the experimental and numerical PGT (Figure 11), LSFA-$\Delta \boldsymbol{x}_{js}$ (Figure 13) and DFA (Figure 15) results to the values of N_{js} or N_{ss} obtained with the techniques in the first column. These results can in fact serve to compare the variability of the X_{susp} values obtained with the PGT, LSFA and DFA techniques. The N_{js} and N_{ss} results are also displayed as a histogram in Figure 21. Note that the values of N_{js} and N_{ss} should not be compared directly as they do not assess the same quantity of suspended particle ($X_{susp} = 1$ vs $X_{sups} = 0.982$, respectively). However, we have judged it pertinent to add the values of N_{js} to Table 5 since it is a more traditional way to look at a solid-liquid mixing system. The value of N_{js} should be higher than the value of N_{ss} and the fraction of suspended solid as measured by any method should be close to 100% at N_{js}.

We can see in Table 5 that the TIA technique greatly underestimates the values of N_{js} with respect to that predicted by the Zwietering correlation, which is $N_{js} = 565$. We note that the correlation put forward by Greenville *et al.* [16] gives a value of $N_{js} = 549$RPM using $z = 1.528$ and $N_p = \frac{P}{\rho N^3 D^5} = 1.55$ (a value obtained using single phase simulations). This result is very similar to the prediction from the Zwiettering correlation.

The value of N_{js} predicted by the Zwiettering correlation is significantly higher than the values of N_{ss} obtained with the other techniques, which is consistent with respect to the definition of N_{js} and N_{ss}. Furthermore, the fraction of suspended solids as measured by the PGT (both experimentally and numerically) at the value of $N_{js} = 565$ is $X_{susp} = 1$, indicating a good agreement between these approaches. The LSFA-$\Delta\boldsymbol{x}$ and DFA results are also in good agreement as they yield fractions of suspended solids of $X_{susp} = 0.999$ and $X_{susp} = 0.993$, respectively, at the value of N_{js} predicted by the Zwietering correlation. These result indicate that the Zwietering correlation gives an accurate assessment of N_{js} for this system, which is not standard as regards the scope of this correlation, due to the rather large size of the particles ($d_p = 0.003m$) and the viscosity of the fluid ($\mu \approx 0.05$).

We note in Figure 21 the good agreement between the PGT (experiments and simulations) and the LSFA-$\Delta\boldsymbol{x}$ and DFA approaches, considering the difficulty in defining adequate time windows for the latter two approaches. More precisely, a very good agreement is be obtained between the PGT and LSFA-$\Delta\boldsymbol{x}$ results for $\Delta t_{js} \in [1, 1.5]$ s, whereas a good agreement between the PGT and DFA results is obtained for $\Delta t_{js} \in [2, 3]$ s. Moreover, we note that these two techniques yield accurate fractions of suspended particles for all impeller speeds, as was shown in Figures 13 and 15, respectively. From a practical point of view, our findings indicate that the PGT, LSFA-$\Delta\boldsymbol{x}$ and DFA techniques are all three suitable when analysing the fraction of suspended solids from Euler-Lagrange

simulations. Although it is accurate and compares very well to experimental data, the PGT technique requires numerous simulation results at various impeller speeds to correct the dynamic pressure. Indeed, this correction can only be calculated when in a fully suspended state. As the impeller speed at which this state is reached is not known a priori, a relatively large number of simulations at various impeller speeds may indeed be needed. On the other hand, the LSFA-$\Delta\boldsymbol{x}$ and DFA approaches can be easily applied to any impeller speed, which is an advantage over the PGT technique as fewer simulations are likely to be required. These two methods are applicable to any vessel geometry, which is not the case of the PGT technique, which requires a flat or conical vessel bottom. Furthermore, these techniques are applied as post-processing techniques using the previously computed CFD-DEM results. Therefore, different sets of parameters for LSFA-$\Delta\boldsymbol{x}$ and DFA can be tried using the same simulation, greatly reducing the computational time. However, it must be noted that the LSFA and DFA techniques require two parametrs and one parameter, respectively. These methods can be used with one single set of parameters to compare the efficiency of different geometries to suspend particles. One should also keep in mind that the quality of the agreement with respect to comparison with experimental results depends up to a certain extent on the choice of these parameters. Furthermore, the results obtained with the LSFA and DFA techniques are less accurate than those obtained using the PGT when compared to the experimental PGT data. Fi-

nally, we note that the generality of these two approaches has yet to be established since only one particle size and one fluid viscosity were investigated in the present work.

Table 5: The first three columns of this table compare the different values of N_{js} and N_{ss} obtained via techniques investigated in this work. The other columns give the fraction of suspended particles X_{susp} as calculated by the PGT (experiments and simulations), LSFA-$\Delta\boldsymbol{x}$ ($\Delta\boldsymbol{x}_{js} = d_p$, $\Delta t_{js} = 1.5$ s) and DFA ($\Delta t_{js} = 2$ s) techniques for the corresponding values of N_{js} or N_{ss} obtained in the second or third column.

			X_{susp}			
Technique or correlation	N_{js}	N_{ss}	Exp. PGT (Figure 11)	Sim. PGT (Figure 11)	LSFA-$\Delta\boldsymbol{x}$ (Figure 13)	DFA (Figure 15)
Zwietering correlation	565	-	100%	100%	99.9%	99.3%
TIA	375	-	87.9%	94.6%	95.7%	95.1%
PGT - Experiments	-	428	98.2%	97.9%	98.6%	97.8%
PGT - Simulations	-	430	98.3%	98.2%	98.6%	97.8%
LSFA-$\Delta\boldsymbol{x}$ ($\Delta\boldsymbol{x}_{js} = d_p$, $\Delta t_{js} = 1.5$ s)	-	416	95.3%	97.8%	98.2%	97.5%
LSFA-Δz ($\Delta\boldsymbol{z}_{js} = d_p$, $\Delta t_{js} = 2$ s)	-	616	100%	100%	100%	99.4%
DFA ($\Delta t_{js} = 2$ s)	-	466	99.3%	99.7%	99.4%	98.2%

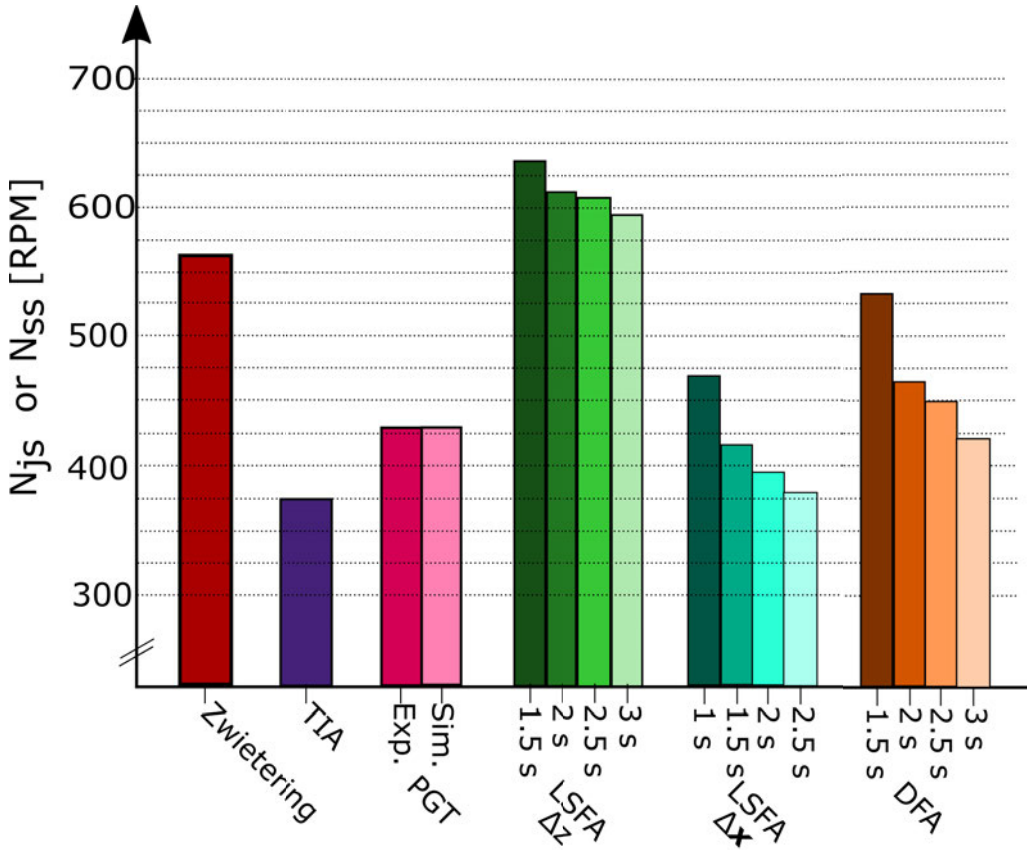

Figure 21: N_{js} or N_{ss} values for the various techniques investigated. The LSFA results are for $\Delta z_{js} = d_p$.

7. Conclusion

730 Predicting the required agitation speed to suspend the desired amount of particles in solid-liquid mixing systems remains a challenging topic of industrial interest. This is not only because of the complex hydrodynamics and the solid-liquid interactions that take place within the agitated vessel, but also because different types of operations (chemical

reactors, crystallizer, etc.) require specific levels of suspension. In particular, the just-suspended speed (N_{js}) is not the adequate operating condition for all processes and may lead to large power over-consumption. The development of novel numerical models, such as those combining CFD for the fluid and DEM for the solid particles, is a promising way to investigate such multiphase systems.

In the present work, we have extended the laminar and transitional solid-liquid mixing model introduced by our group [25], based on the CFDEM framework (combining LIGGGHTS and Open∇FOAM), to turbulent flows by means of LES. Numerous techniques to measure the just-suspended speed (or the sufficiently suspended speed N_{ss} as an approximation) as well as the fraction of suspended particles were discussed. Two new approaches, the Lagrangian suspended fraction analysis (in two variants, LSFA-$\Delta\boldsymbol{x}$ and LSFA-Δz) and decorrelated fraction analysis (DFA) techniques, were introduced. Both methods are global metrics based on the analysis of the time-dependent position of each particle. While the LSFA technique is based directly on the displacement of the particles, the DFA technique relies on a mixing index developed in our group [79] to analyze the loss of correlation of the positions of the particles with respect to their initial positions. Thus, it also assesses the mixing efficiency.

A standard set-up consisting of a baffled stirred tank equipped with a PBT and filled with a non-dilute concentration ($10wt\%$) of glass beads was studied. The PBT was

found to behave much like an axial discharge impeller with single loop patterns. It was also observed that the particle Reynolds number was significant only close to specific elements of the geometry (vessel bottom, baffles, impeller) and that in other location in the tank, the particle velocity was close to that of the fluid. Analysis of solid concentration profiles highlighted zones of particle accumulation at the bottom-wall junction, which was corroborated by our experimental observations.

The fraction of suspended particles was investigated theoretically via the Zwietering correlation, experimentally using the pressure gauge technique (PGT) and via CFD-DEM using a variety of numerical techniques: pressure gauge, LSFA-Δz, LSFA-$\Delta \boldsymbol{x}$, DFA, TIA, power consumption, local particle concentration and transient solids concentration. No usable results could be obtained with the latter three approaches. In fact, this revealed the lack of generality of these methods. An excellent agreement was obtained between the experimental and numerical PGT N_{ss} results, which validated the accuracy of the unresolved CFD-DEM model proposed in this work.

The Zwietering correlation predicted a value of $N_{js} = 565$RPM, which was above the values for N_{ss}. At this speed, the PGT predicted full suspension both experimentally and numerically. Thus, the Zwiettering correlation was in good agreement with the simulation and experimental results obtained in this work. The LSFA-Δz was found to overpredict the value of N_{ss} when compared to the PGT. However, a good agreement was obtained

between the LSFA-$\Delta \boldsymbol{x}$ and the PGT. A good agreement was also observed with the DFA technique, although this required a larger observation time $\Delta t_{js} \geq 2$ s. These two techniques, as well as the pressure gauge technique, are highly promising because they provide a global assessment of the suspension of the particles and are based on physical grounds very close to Zwietering's original definition. Furthermore, both the LSFA-$\Delta \boldsymbol{x}$ and DFA techniques can assess the fraction of suspended particles at a given velocity with only one simulation contrary to the PGT technique that requires many simulations to remove the dynamic component from the total pressure curve. This renders their use far less time-consuming and less error-prone due to the absence of the dynamic pressure correction. Furthermore, they are suitable for all kinds of vessels, contrary to the PGT technique which works only with flat-bottomed or conical vessels. However, the LSFA and DFA methods require 2 parameters and 1 parameter respectively, which makes these methods more subjective when they are not used to compare the efficiency of geometries to suspend particles.

Due to its accurate resolution of the particle dynamics and tractable overall computational times, the unresolved CFD-DEM model proposed in this work paves the way to a new generation of models for solid-liquid mixing.

8. Acknowledgements

The financial support from the Natural Sciences and Engineering Research Council of Canada (NSERC) is gratefully acknowledged. In particular, Bruno Blais is thankful for the NSERC Vanier Scholarship. The authors would like to thank Gilles Lenfant for the rheological measurements of the glucose solution and Manon Lassaigne for fruitful discussion on the design of experiments. Computations were made on supercomputer Colosse from the University Laval, managed by Calcul Québec. In particular, the authors would like to acknowledge the efficient support received from Calcul Québec systems analysts.

References

[1] E. L. Paul, V. A. Atiemo-Obeng, S. M. Kresta, Handbook of Industrial Mixing - Science and Practice (2004).

[2] F. Kneule, Die prüfung von rührern durch löslichkeitsbestimmung, Chemie Ingenieur Technik 28 (3) (1956) 221–225.

[3] A. W. Nienow, M. F. Edwards, N. Harnby, Mixing in the process industries, Butterworth-Heinemann, 1997.

[4] T. N. Zwietering, Suspending of solid particles in liquid by agitators, Chemical Engineering Science 8 (3) (1958) 244–253.

[5] G. R. Kasat, A. B. Pandit, Review on mixing characteristics in solid-liquid and solid-liquid-gas reactor vessels, Canadian Journal of Chemical Engineering 83 (4) (2005) 618–643.

[6] R. Jafari, P. A. Tanguy, J. Chaouki, Experimental investigation on solid dispersion, power consumption and scale-up in moderate to dense solid-liquid suspensions, Chemical Engineering Research & Design 90 (2) (2012) 201–212.

[7] M. Lassaigne, B. Blais, L. Fradette, F. Bertrand, Experimental investigation of the mixing of viscous liquids and non-dilute concentrations of particles in stirred tanks, Submitted to Chemical Engineering Research & Design (2015) .

[8] S. B. Ibrahim, A. W. Nienow, The effect of viscosity on mixing pattern and solid suspension in stirred vessels, Eighth European Conference on Mixing (136) (1994) 25–32.

[9] S. Ibrahim, A. W. Nienow, Comparing impeller performance for solid-suspension in the transitional flow regime with Newtonian fluids, Chemical Engineering Research and Design 77 (8) (1999) 721–727.

[10] I. Ayranci, S. M. Kresta, Critical analysis of Zwietering correlation for solids suspension in stirred tanks, Chemical Engineering Research and Design 92 (3) (2014) 413–422.

[11] I. Ayranci, S. M. Kresta, Design rules for suspending concentrated mixtures of solids in stirred tanks, Chemical Engineering Research & Design 89 (10A) (2011) 1961–1971.

[12] A. W. Nienow, Suspension of solid particles in turbine agitated baffled vessels, Chemical Engineering Science 23 (12) (1968) 1453–1459.

[13] S. Narayanan, V. K. Bhatia, D. K. Guha, M. N. Rao, Suspension of solids by mechanical agitation, Chemical Engineering Science 24 (2) (1969) 223–230.

[14] G. Baldi, R. Conti, E. Alaria, Complete suspension of particles in mechanically agitated vessels, Chemical Engineering Science 33 (1) (1978) 21–25.

[15] A. Mersmann, F. Werner, S. Maurer, K. Bartosch, Theoretical prediction of the minimum stirrer speed in mechanically agitated suspensions, Chemical Engineering and Processing 37 (6) (1998) 503–510.

[16] R. Grenville, A. Mak, D. Brown, Suspension of solid particles in vessels agitated by axial flow impellers, Chemical Engineering Research and Design (2015) .

[17] A. Tamburini, A. Brucato, A. Busciglio, A. Cipollina, F. Grisafi, G. Micale, F. Scargiali, G. Vella, Solid–liquid suspensions in top-covered unbaffled vessels: Influence of particle size, liquid viscosity, impeller size, and clearance, Industrial & Engineering Chemistry Research 53 (23) (2014) 9587–9599.

[18] J. Oldshue, R. Sharma, The effect of off-bottom distance of an impeller for the "Just Suspended Speed" Njs, in: AIChE Symposium Series, Vol. 88, American Institute of Chemical Engineers, 1992, pp. 72–72.

[19] A. Tamburini, A. Cipollina, G. Micale, A. Brucato, M. Ciofalo, CFD simulations of dense solid-liquid suspensions in baffled stirred tanks: Prediction of suspension curves, Chemical Engineering Journal 178 (2011) 324–341.

[20] A. Brucato, V. Brucato, Unsuspended mass of solid particles in stirred tanks, The Canadian Journal of Chemical Engineering 76 (3) (1998) 420–427.

[21] J. Y. Oldshue, Fluid mixing technology.

[22] A. Brucato, G. Micale, L. Rizzuti, Determination of the amount of unsuspended solid particles inside stirred tanks by means of pressure measurements, Récent Progrès Génie des Procédés 11 (1997) 3–10.

[23] G. Micale, F. Grisafi, A. Brucato, Assessment of particle suspension conditions in stirred vessels by means of pressure gauge technique, Chemical Engineering Research and Design 80 (8) (2002) 893–902.

[24] A. Tamburini, A. Brucato, A. Cipollina, G. Micale, M. Ciofalo, CFD predictions of sufficient suspension conditions in solid-liquid agitated tanks, International Journal of Nonlinear Sciences and Numerical Simulation 13 (6) (2012) 427–443.

[25] B. Blais, M. Lassaigne, C. Goniva, L. Fradette, F. Bertrand, Development of an unresolved CFD–DEM model for the flow of viscous suspensions and its application to solid–liquid mixing, Journal of Computational Physics 318 (2016) 201–221.

[26] G. Micale, G. Montante, F. Grisafi, A. Brucato, J. Godfrey, CFD simulation of particle distribution in stirred vessels, Chemical Engineering Research & Design 78 (A3) (2000) 435–444.

[27] M. Ljungqvist, A. Rasmuson, Numerical simulation of the two-phase flow in an axially stirred vessel, Chemical Engineering Research & Design 79 (A5) (2001) 533–546.

[28] G. Micale, F. Grisafi, L. Rizzuti, A. Brucato, CFD simulation of particle suspension height in stirred vessels, Chemical Engineering Research & Design 82 (A9) (2004) 1204–1213.

[29] G. Montante, F. Magelli, Modelling of solids distribution in stirred tanks: Analysis of simulation strategies and comparison with experimental data, International Journal of Computational Fluid Dynamics 19 (3) (2005) 253–262.

[30] A. Ochieng, A. E. Lewis, CFD simulation of solids off-bottom suspension and cloud height, Hydrometallurgy 82 (1-2) (2006) 1–12.

[31] G. R. Kasat, A. R. Khopkar, V. V. Ranade, A. B. Pandita, CFD simulation of liquid-

phase mixing in solid-liquid stirred reactor, Chemical Engineering Science 63 (15) (2008) 3877–3885.

[32] G. Montante, F. Magelli, Mixed solids distribution in stirred vessels: Experiments and computational fluid dynamics simulations, Industrial & Engineering Chemistry Research 46 (9) (2007) 2885–2891.

[33] A. Tamburini, A. Cipollina, G. Micale, M. Ciofalo, A. Brucato, Dense solid-liquid off-bottom suspension dynamics: Simulation and experiment, Chemical Engineering Research and Design 87 (4) (2009) 587–597.

[34] S. Hosseini, D. Patel, F. Ein-Mozaffari, M. Mehrvar, Study of solid-liquid mixing in agitated tanks through computational fluid dynamics modeling, Industrial & Engineering Chemistry Research 49 (9) (2010) 4426–4435.

[35] A. Tamburini, A. Cipollina, G. Micale, CFD simulation of solid-liquid suspensions in baffled stirred vessels below complete suspension speed, ICHEAP-10: 10th International Conference on Chemical and Process Engineering 24 (2011) 1435–1440.

[36] A. Tamburini, A. Cipollina, G. Micale, A. Brucato, M. Ciofalo, CFD simulations of dense solid-liquid suspensions in baffled stirred tanks: Prediction of the minimum impeller speed for complete suspension, Chemical Engineering Journal 193 (2012) 234–255.

[37] A. Tamburini, A. Cipollina, G. Micale, A. Brucato, M. Ciofalo, CFD simulations of dense solid–liquid suspensions in baffled stirred tanks: Prediction of solid particle distribution, Chemical Engineering Journal 223 (2013) 875–890.

[38] F. Wang, Z. S. Mao, X. Q. Shen, Numerical study of solid-liquid two-phase flow in stirred tanks with Rushton impeller - (II) Prediction of critical impeller speed, Chinese Journal of Chemical Engineering 12 (5) (2004) 610–614.

[39] V. B. Rewatkar, K. S. M. S. R. Rao, J. B. Joshi, Critical impeller speed for solid suspension in mechanically agitated 3-phase reactors .1. experimental part, Industrial & Engineering Chemistry Research 30 (8) (1991) 1770–1784.

[40] K. Raghava Rao, V. Rewatkar, J. Joshi, Critical impeller speed for solid suspension in mechanically agitated contactors, AIChE journal 34 (8) (1988) 1332–1340.

[41] A. Brucato, F. Grisafi, G. Montante, Particle drag coefficients in turbulent fluids, Chemical Engineering Science 53 (18) (1998) 3295–3314.

[42] D. Pinelli, M. Nocentini, F. Magelli, Solids distribution in stirred slurry reactors: influence of some mixer configurations and limits to the applicability of a simple model for predictions, Chemical Engineering Communications 188 (1) (2001) 91–107.

[43] J. J. Derksen, Numerical simulation of solids suspension in a stirred tank, AIChE Journal 49 (11) (2003) 2700–2714.

[44] T. Shao, Y. Hu, W. Wang, Y. Jin, Y. Cheng, Simulation of solid suspension in a stirred tank using CFD-DEM coupled approach, Chinese Journal of Chemical Engineering 21 (10) (2013) 1069–1081.

[45] CFDEM, CFDEM- Open Source CFD, DEM and CFD-DEM, URL : http://www.cfdem.com, 2015.

[46] C. Goniva, C. Kloss, N. G. Deen, J. A. M. Kuipers, S. Pirker, Influence of rolling friction on single spout fluidized bed simulation, Particuology 10 (5) (2012) 582–591.

[47] OpenCFD, OpenFOAM - The Open Source CFD Toolbox, URL : http://www.openfoam.com, 2014.

[48] LIGGGHTS, LAMMPS Improved for General Granular and Granular Heat Transfer Simulations, URL : hhttp://www.liggghts.com, 2015.

[49] C. Kloss, C. Goniva, LIGGGHTS Open Source Discrete Element Simulations of Granular Materials Based on Lammps, John Wiley & Sons, Inc., 2011, pp. 781–788, (TMS).

[50] R. B. Thorpe, P. Stevenson, Suspension of particles from the bottom of pipes and

stirred tanks by gassed and ungassed flows, Canadian Journal of Chemical Engineering 81.

[51] B. Blais, M. Lassaigne, C. Goniva, L. Fradette, F. Bertrand, A semi-implicit immersed boundary method and its application to viscous mixing, Computers & Chemical Engineering 85 (2016) 136–146.

[52] J. Capecelatro, O. Desjardins, An Euler–Lagrange strategy for simulating particle-laden flows, Journal of Computational Physics 238 (2013) 1–31.

[53] T. Anderson, R. Jackson, A fluid mechanical description of fluidized beds, Ind. Engng Chem. Fundam. 6 (1967) 527–539.

[54] Z. Y. Zhou, S. B. Kuang, K. W. Chu, A. B. Yu, Discrete particle simulation of particle-fluid flow: model formulations and their applicability, Journal of Fluid Mechanics 661 (2010) 482–510.

[55] F. Bertrand, L. A. Leclaire, G. Levecque, DEM-based models for the mixing of granular materials, Chemical Engineering Science 60 (8-9) (2005) 2517–2531.

[56] H. P. Zhu, Z. Y. Zhou, R. Y. Yang, A. B. Yu, Discrete particle simulation of particulate systems: Theoretical developments, Chemical Engineering Science 62 (13) (2007) 3378–3396.

[57] Y. Tsuji, T. Tanaka, T. Ishida, Lagrangian numerical-simulation of plug flow of cohesionless particles in a horizontal pipe, Powder Technology 71 (3) (1992) 239–250.

[58] K. Johnson, Normal contact of elastic solids: Hertz theory, Contact Mechanics (1985) 84–106.

[59] H. Hertz, ber die berhung fester elasticher krpe, Journal fur die reine und angewandte Mathematik (1882) 156–171.

[60] R. D. Mindlin, H. Deresiewica, Elastic spheres in contact under varying oblique forces, Journal of applied mechanics 20.

[61] R. Mindlin, Compliance of elastic bodies in contact, J. of Appl. Mech. 16.

[62] D. Gidaspow, Multiphase Flow and Fluidization: Continuum and Kinetic Theory Descriptions, Academic press, 1994.

[63] P. Sagaut, Large Eddy Simulation for Incompressible Flows, Springer, 2006.

[64] J. H. Ferziger, M. Perić, Computational methods for fluid dynamics, Vol. 3, Springer Berlin, 1996.

[65] S. B. Pope, Turbulent flows, Cambridge university press, 2000.

[66] R. I. Issa, Solution of the implicitly discretised fluid flow equations by operator-splitting, Journal of Computational Physics 62 (1) (1986) 40–65.

[67] B. Blais, F. Bertrand, On the use of the method of manufactured solutions for the verification of CFD codes for the volume-averaged Navier–Stokes equations, Computers & Fluids 114 (2015) 121–129.

[68] L. W. Rong, K. J. Dong, A. B. Yu, Lattice-Boltzmann simulation of fluid flow through packed beds of uniform spheres: Effect of porosity, Chemical Engineering Science 99 (2013) 44–58.

[69] R. Mei, An approximate expression for the shear lift force on a spherical particle at finite reynolds number, International Journal of Multiphase Flow 18 (1) (1992) 145–147.

[70] E. Loth, A. Dorgan, An equation of motion for particles of finite reynolds number and size, Environmental fluid mechanics 9 (2) (2009) 187–206.

[71] J. B. McLaughlin, Inertial migration of a small sphere in linear shear flows, Journal of Fluid Mechanics 224 (1991) 261–274.

[72] E. Loth, Lift of a spherical particle subject to vorticity and/or spin, Aiaa Journal 46 (4) (2008) 801–809.

[73] C. Crowe, J. D. Schwartzkopf, M. Sommerfeld, Y. Tsuji, Multiphase Flows with Droplets and Particles Flows, CRC Press, 2012.

[74] B. Oesterle, T. B. Dinh, Experiments on the lift of a spinning sphere in a range of intermediate reynolds numbers, Experiments in Fluids 25 (1) (1998) 16–22.

[75] S. Dennis, S. Singh, D. Ingham, The steady flow due to a rotating sphere at low and moderate reynolds numbers, Journal of Fluid Mechanics 101 (02) (1980) 257–279.

[76] S. K. Arolla, O. Desjardins, Transport modeling of sedimenting particles in a turbulent pipe flow using euler–lagrange large eddy simulation, International Journal of Multiphase Flow 75 (2015) 1–11.

[77] S. Pirker, D. Kahrimanovic, C. Goniva, Improving the applicability of discrete phase simulations by smoothening their exchange fields, Applied Mathematical Modelling 35 (5) (2011) 2479–2488.

[78] J. Marshall, K. Sala, Comparison of methods for computing the concentration field of a particulate flow, International Journal of Multiphase Flow 56 (2013) 4–14.

[79] J. Doucet, F. Bertrand, J. Chaouki, A measure of mixing from lagrangian tracking and its application to granular and fluid flow systems, Chemical Engineering Research and Design 86 (12) (2008) 1313–1321.

[80] J. Shlens, A tutorial on principal component analysis, arXiv preprint arXiv:1404.1100.

[81] B. Blais, F. Bertrand, Cfd-dem investigation of the viscous solid-liquid mixing in agitated vessels: impact of particle properties and mixer characteristics, In preparation.

[82] J. Bourne, R. Sharma, Suspension characteristics of solid particles in propeller-agitated tanks, in: Proceedings of the First European Conference on Mixing and Centrifugal Separation, Cambridge, Vol. 3, BHRA Cranfield, UK, 1974, pp. 25–39.

[83] N. C. S. Kee, R. B. H. Tan, CFD simulation of solids suspension in mixing vessels, Canadian Journal of Chemical Engineering 80 (4) (2002) 721–726.

[84] M. Micheletti, L. Nikiforaki, K. C. Lee, M. Yianneskis, Particle concentration and mixing characteristics of moderate-to-dense solid-liquid suspensions, Industrial & engineering chemistry research 42 (24) (2003) 6236–6249.

[85] A. Di Renzo, F. P. Di Maio, Homogeneous and bubbling fluidization regimes in DEM-CFD simulations: Hydrodynamic stability of gas and liquid fluidized beds, Chemical Engineering Science 62 (1-2) (2007) 116–130.

[86] A. Di Renzo, F. Cello, F. P. Di Maio, Simulation of the layer inversion phenomenon in

binary liquid-fluidized beds by DEM-CFD with a drag law for polydisperse systems, Chemical Engineering Science 66 (13) (2011) 2945–2958.